CrossMark

RESEARCH ARTICLE

Column-integrated aerosol optical properties and direct radiative forcing over the urban-industrial megacity Nanjing in the Yangtze River Delta, China

Na Kang[1] · K. Raghavendra Kumar[1] · Xingna Yu[1] · Yan Yin[1]

Abstract Aerosol optical properties were measured and analyzed through the ground-based remote sensing Aerosol Robotic Network (AERONET) over an urban-industrial site, Nanjing (32.21° N, 118.72° E, and 62 m above sea level), in the Yangtze River Delta, China, during September 2007–August 2008. The annual averaged values of aerosol optical depth (AOD_{500}) and the Ångström exponent ($AE_{440-870}$) were measured to be 0.94 ± 0.52 and 1.10 ± 0.21, respectively. The seasonal averaged values of AOD_{500} ($AE_{440-870}$) were noticed to be high in summer (autumn) and low in autumn (spring). The characterization of aerosol types showed the dominance of mixed type followed by the biomass burning and urban-industrial type of aerosol at Nanjing. Subsequently, the curvature (a_2) obtained from the second-order polynomial fit and the second derivative of AE (α') were also analyzed to understand the dominant aerosol type. The single scattering albedo at 440 nm (SSA_{440}) varied from 0.88 to 0.93 with relatively lower (higher) values during the summer (spring), suggesting an increase in black carbon and mineral dust (desert dust) aerosols of absorbing (scattering) nature. The averaged monthly and seasonal evolutions of shortwave (0.3–4.0 μm) direct aerosol radiative forcing (DARF) values were computed from the Santa Barbara DISORT Atmospheric Radiative Transfer (SBDART) model both at the top of atmosphere (TOA) and bottom of atmosphere (SUR) during the study period. Further, the aerosol forcing efficiency (AFE) and the corresponding atmospheric heating rates (AHR) were also estimated from the forcing within the atmosphere (ATM). The derived DARF values, therefore, produced a warming effect within the atmosphere due to strong absorption of solar radiation.

Introduction

Aerosols are important atmospheric components, and the way they influence regional and global climate change is not well understood (Ramanathan et al. 2001). They alter the radiative balance of the atmosphere directly by absorbing and scattering solar radiation and indirectly by changing the microphysical properties of cloud and precipitation efficiency (acting as cloud condensation nuclei) (Twomey et al. 1984). Current understanding of aerosol's direct and indirect effects remains highly uncertain, constituting the greatest uncertainty in climate prediction (IPCC 2013). The role of aerosols is dependent on their physical, chemical, and optical properties as well as complex aerosol processes and their interactions in the atmosphere (Jacobson 2001), which vary significantly in space and time. The aerosol optical and physical properties such as aerosol optical depth (AOD), Ångström exponent (AE), and

✉ K. Raghavendra Kumar
kanike.kumar@gmail.com; krkumar@nuist.edu.cn

[1] Key Laboratory of Meteorological Disaster, Ministry of Education (KLME)/International Joint Laboratory on Climate and Environmental Change (ILCEC)/Collaborative Innovation Center on Forecast and Evaluation of Meteorological Disasters/Key Laboratory for Aerosol-Cloud-Precipitation of China Meteorological Administration, School of Atmospheric Physics, Nanjing University of Information Science and Technology, Nanjing 210044, Jiangsu, China

single scattering albedo (SSA) are important parameters that control the direct aerosol radiative forcing (DARF) at the surface (SUR) and at the top of the atmosphere (TOA) (Holben et al. 1998).

Satellite and ground-based remote sensing techniques are the most essential tools used and mainly adapted to measure aerosol optical properties and the radiative effects that aerosols have on climate (Charlson et al. 1992). Among these two, ground-based remote sensing has become a powerful method for characterizing atmospheric aerosols (Dubovik and King 2000) and has been widely used due to its simplicity and accuracy. Based on the sun-sky radiometers in different regions of the world, several ground-based observation networks, such as Aerosol Robotic Network (AERONET) (Holben et al. 1998), Photométrie pour le Traitement Opérationnel de Normalisation Satellitaire (PHOTONS) (Goloub et al. 2007), China Aerosol Remote Sensing Network (CARSNET) (Che et al. 2009), and Skyradiometer Network (SKYNET) (Takemura and Nakajima 2004) have been developed to study regional aerosol optical properties and validate satellite retrievals.

During the recent decades, China has experienced unprecedented economic development due to extensive urbanization and industrialization and an increase of population and traffic (Deng et al. 2012; Wang et al. 2015; Yu et al. 2016a, b). It is also known that China is one of the largest source regions for anthropogenic aerosols in the world (e.g., Xia et al. 2013; Wang et al. 2015; Yu et al. 2016c). East China, particularly Nanjing and Shanghai in the Yangtze River Delta (YRD), is a fast developing and densely populated region, where anthropogenic emissions of particles and gaseous precursors have been increasing significantly over recent decades (Li et al. 2015; Cheng et al. 2015; Yu et al. 2016a). With the region being located on the west coast of the Pacific Ocean, the largest industrial and agriculture productive areas suffer with severe biomass burning (Pan et al. 2010; Deng et al. 2012). High concentrations of particular matter, poor air quality, and visibility degradation are due to complex pollutant emission with the rapid economic development and population growth in China. This has brought serious environmental damage and degradation of human health. It has also greatly affected the changes in weather conditions and led to frequent occurrences of severe haze-fog episodes over urban regions (Pan et al. 2010; Cheng et al. 2015).

Numerous observations have been carried out in the past few years to study aerosol optical properties and associated DARF effects in different regions of China (Pan et al. 2010; Wang et al. 2010, 2015; Chen et al. 2012; Liu et al. 2012; Li et al. 2015; Xia et al. 2016; Cheng et al. 2015; Wu et al. 2015; Yu et al. 2016b, c). Pan et al. (2010) compared aerosol optical properties measured by sun photometer at five sites. Wang et al. (2015) exhibited aerosol optical properties retrieved from the long-term (2007–2013) continuous measurements

of sun photometer in urban Wuhan. They found that AOD_{500} has its highest values of 1.52 which occurred in summer (June) 2012 and the lowest (0.57) in winter (November) 2012. Similarly, Li et al. (2015) noticed a maximum AOD_{440} in August (1.22) and a minimum in February (0.51) from sun photometer measurements at Nanjing analyzed during April 2011–April 2012. Further, Cheng et al. (2015) also characterized columnar and surface aerosol properties over highly polluted urban station of Shanghai from December 2010 to October 2012. Recently, the aerosol optical properties and associated DARF (shortwave and longwave) were investigated by Yu et al. (2016c) over urban Beijing during severe dust storm conditions from 2001 to 2014. However, the observation of aerosol optical properties in the YRD region is still deficient, and none of them focused on the spectral dependence of the aerosol optical properties and model simulated DARF of urban aerosols.

The present investigation attempts to delineate the seasonally varying contribution of natural and anthropogenic aerosols emitted from various sources based on the spectral distribution of optical characteristics of aerosols. In this paper, the observation data measured from the AERONET sun photometer during September 2007–August 2008 has been used to study the changes in the aerosol optical properties and associated DARF over urban Nanjing in the YRD, China. Here we examined the aerosol optical and radiative properties in terms of AOD, AE, volume size distribution (VSD), SSA, and asymmetry parameter (ASY), together with the real (Re) and imaginary (Im) parts of aerosol complex refractive index (RI). Further, the monthly and seasonal averaged values of DARF and aerosol forcing efficiency (AFE) at the SUR and the TOA are computed using the Santa Barbara DISORT Atmospheric Radiative Transfer (SBDART) model (Ricchiazzi et al. 1998). The estimated DARF and AFE values are compared with those magnitudes derived from AERONET to know the radiative and climatic impacts at Nanjing. The structure of the paper is organized as follows. Site details, data, and methodology are described in the "Measurement and methods" section. The "Results and discussion" section presents monthly and seasonal variations of aerosol optical and radiative properties, and estimation of DARF. Finally, the main conclusions are provided in the last section. To avoid confusion for the readers, the nomenclature of derived parameters used in the present study and their abbreviations with units is given in Table S1 of Supplementary material (SM).

Measurement and methods

Site description

Nanjing, the capital city of Jiangsu Province, is located in the north of the Jianghuai Plain and northwest of the YRD.

Nanjing, a megacity, is the second largest center of economy and culture in East China after Shanghai, whose urban atmosphere can be heavily polluted by local emissions and long-range transport (Li et al. 2015; Yu et al. 2016a). With the rapid development of industry and economy, the air quality in Nanjing is attracting more and more attention (e.g., Pan et al. 2010; Zhuang et al. 2014; Li et al. 2015; Yu et al. 2016a). Aerosol observations were carried out on the roof of the Meteorology Building about 50 m above the ground level within the campus of Nanjing University of Information Science and Technology (NUIST; lat 32.21° N, long 118.72° E, and elevation 62 m above sea level) in the northern suburb of Nanjing. The location of the observation site is shown in Fig. 1 indicating the site and the major pollution sources surrounding it. The Nanjing Chemical Industry is located approximately 3 km to the southeast of the observation site. In addition, there are iron and steel plants, as well as coal generation power plants within the 1-km vicinity of the measurement site.

Also, there is a road way approximately 500 m to the east of the observation site (see Fig. 1). Thus, local contributions to air particles are derived from the combination of vehicular traffic, urbanization, industries, and crop land sources.

Local meteorology

The 24-h daily average meteorological parameters were procured from http://wunderground.com, a World Wide Web-based meteorological variables for a geographical area and previously been used by other researchers (Alam et al. 2011; Srivastava et al. 2015; Kumar et al. 2015). Depending on the prevailing meteorological conditions over Nanjing, a year can be broadly divided into four distinct seasons, namely winter (December–January–February; DJF), spring (March–April–May; MAM), summer (June–July–August; JJA), and autumn (September–October–November; SON) (Zhuang et al. 2014). The monthly mean meteorological parameters including
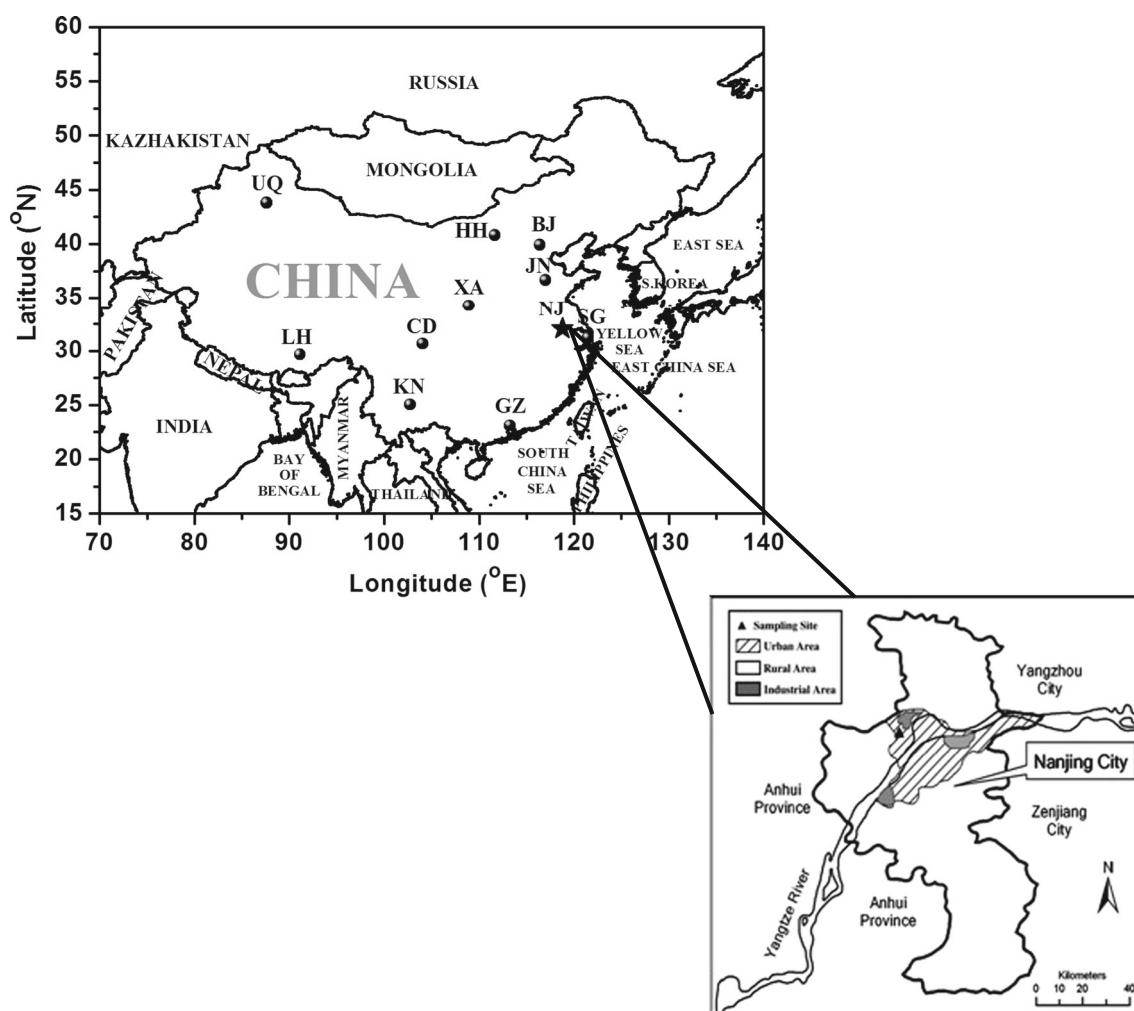

Fig. 1 Geographical location of Nanjing (*NJ*) over China represented with a *solid star symbol* along with its bordering countries and oceans. Also shown is the location of NJ urban-industrial area indicated with a triangle in the Yangtze River Delta (YRD) with its major sources in the vicinity of the sampling site. The major urban areas of China are also noted that influence the air quality of NJ. *BJ* Beijing, *HH* Hohhot, *JN* Jinan, *UQ* Urumqi, *CD* Chengdu, *XA* Xian, *SG* Shanghai, *LH* Lhasa, *KN* Kunming, *GZ* Guangzhou

temperature (Temp), relative humidity (RH), visibility (Vis), rainfall (RF), and wind speed (WS) for the period September 2007–August 2008 are illustrated in Fig. 2. The temperature of Nanjing varied from a minimum value of 1–6 °C in winter to a maximum of 24–30 °C in summer (see Fig. 2a). The RH, shown as the color of data points for temperature with the corresponding color scale provided adjacent to Fig. 2a, varied with a high value of 70–80 % during summer and low values between 63 and 68 % during autumn, whereas the visibility was decreased in winter (5–10 km) with increase in RH (80 %) (Fig. 2b). The maximum WS of 4–7 m s^{-1} was recorded in spring and minimum of 2–4 m s^{-1} in autumn and winter (Fig. 2c). The annual RF presented in Fig. 2d at Nanjing during the study period is of the order of 644 mm with minimum and maximum shares during the autumn (51 mm) and summer (330 mm) seasons, respectively. The averaged Temp, RH, Vis, and WS recorded during the entire period of the study at Nanjing were 16 °C, 74 %, 10 km, and 5 m s^{-1}, respectively. Therefore, on the basis of meteorology, aerosol properties are grouped into four major seasons as mentioned above.

Instrument and method

The observations were conducted using a ground-based automatic sun-sky radiometer (CE-318) of Cimel Electronique installed on the roof of the observation site (NUIST) during September 2007–August 2008. The sun photometer measures direct solar radiance across eight channels from the near-infrared to ultraviolet at 340, 380, 440, 500, 675, 870, 1020, and 940 nm with a 1.2° full field-of-view (Holben et al. 1998). Measurements on the first seven channels are used to retrieve the AOD, with those at 940 nm used to retrieve precipitable

water vapor (PWV) in the atmosphere. All filters for standard sun photometer are narrow bands with the bandwidth of 10 nm, except for 380 and 340 nm with bandwidth of 2 nm. The sky radiance observations from almucantar scans at 440, 675, 870, and 1020 nm are used to retrieve the column-integrated aerosol optical and microphysical properties such as SSA, ASY, complex RI (Re and Im), and VSD (Dubovik and King 2000; Dubovik et al. 2002). Note that only the SSA and complex RI of almucantar retrievals with AOD at 440 (AOD$_{440}$) >0.4 are retained in this study, to avoid the large inversion errors from the limited information content when AOD$_{440}$ <0.4 (Dubovik and King 2000). The retrieval accuracy, calibration, and uncertainties have been discussed by several earlier authors (Dubovik and King 2000; Dubovik et al. 2002; Alam et al. 2011, 2012; Adesina et al. 2014; Xia et al. 2013; Che et al. 2014; Wu et al. 2015; Cheng et al. 2015; Yu et al. 2016b, c) and hence not discussed here to avoid repetition.

The AERONET data are available at three levels (Holben et al. 1998; Smirnov et al. 2000) and can be downloaded from the AERONET website (http://aeronet.gsfc.nasa.gov/). Level 1.5 data (cloud-screened only) from September 2007 to August 2008 that was downloaded from the NUIST site (part of AERONET) has been used in this study. This level of data was also used previously by several other researchers (e.g., Alam et al. 2012; Tiwari et al. 2015) due to unavailability or not released of level 2.0 data (cloud-screened with quality assured) by the AERONET. This year was chosen due to the continuous availability of the dataset (except for the months from November 2007 to February 2008) on the AERONET website, allowing us to study the seasonal variations of different parameters with respect to meteorology. The missing of data may be due to the malfunction in the instrument and/or

Fig. 2 Monthly mean variations of meteorological parameters: **a** temperature, **b** visibility, **c** wind speed, and **d** total rainfall observed at Nanjing. Temperature and visibility are shown as a function of relative humidity (*RH*) representing RH as the color of the data points and the color scale is shown on the *right side* of the corresponding panels
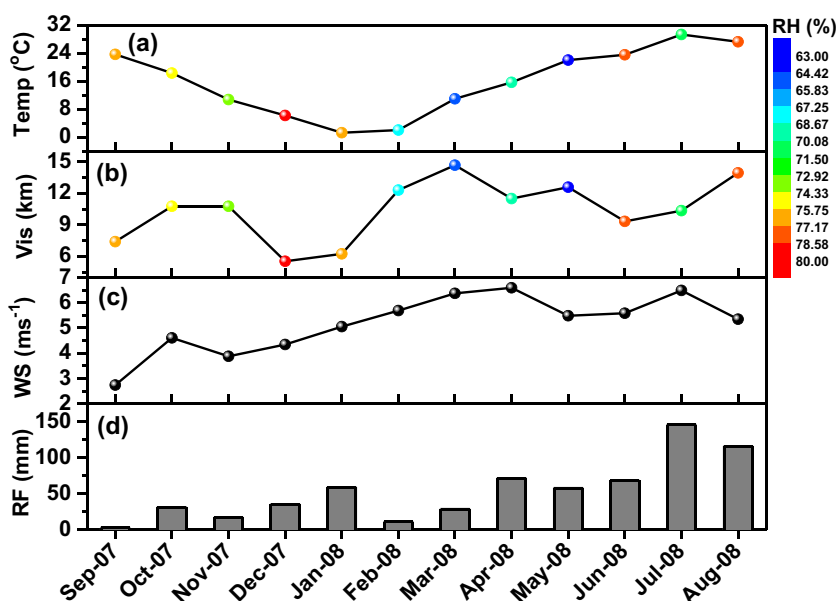
sent for calibration, which restricts the complete usage of data during the winter over Nanjing. Also, there is a little data for September 2007 (6 days) and it is not possible to retrieve inversion products. More data are obtained during spring and summer seasons, mainly due to the sunny days and better weather conditions.

The Moderate Resolution Imaging Spectroradiometer (MODIS) data on board the Terra satellite level 3 aerosol products with spatial resolution of $1° \times 1°$ obtained from NASA GIOVANNI were also used in this paper. Remer et al. (2005) estimated the uncertainty of $\pm 0.05 \pm 0.15$(AOD) for MODIS AOD over land. Other research also used the MODIS AOD retrieval error of $\pm 0.05 \pm 0.2$(AOD) (Tanre et al. 2001) over ocean. More detailed information on algorithms for the retrieval of aerosol products is available at http://modis-atmos.gsfc.nasa.gov.

Ångström exponent and its derivative

Spectral variation of AOD can be represented by Ångström power law ($\tau = \beta \lambda^{-\alpha}$, where τ is AOD, λ is the wavelength in micrometers, and α and β are Ångström parameters) (Angstrom 1964). AE (or α) is calculated from the linear fit of lnAOD versus $\ln\lambda$ data and is known as the Ångström wavelength exponent. β is the turbidity coefficient which is equal to the AOD at a wavelength of 1 μm. The AE value depends on aerosol particle size and varies from 1 to 3 for fresh and aged smoke, and for urban aerosol particles, while AE is nearly zero for coarse-mode aerosols such as dust and sea salt (Eck et al. 1999). β ranges between 0 and 1 and is an indicator of the amount of aerosols present in the atmospheric column. In the ambient atmosphere, aerosol size distribution is multimodal with contribution from both fine- and coarse-mode aerosols and departs from the Junge power law, on which the Ångström formula is used (Angstrom 1964). Therefore, the Ångström power law can introduce significant errors in the determination of aerosol size distribution (Eck et al. 1999). Under these conditions, deviation from linear behavior of lnAOD versus $\ln\lambda$ data occurs, which can be quantified by fitting a second-order polynomial represented as

$$\ln\tau_\lambda = a_2(\ln\lambda)^2 + a_1(\ln\lambda) + a_0 \tag{1}$$

where a_0, a_1, and a_2 are the coefficients often observed in sun photometer measurements. The coefficient a_2 accounting for the curvature can be an indicator of the aerosol particle size, with negative and positive values indicating aerosol size distributions dominated by fine- and coarse-mode aerosols, respectively (Eck et al. 1999; Schuster et al. 2006). The second-order polynomial fit

shown in Eq. (1) was applied to the AOD values at four wavelengths (440, 500, 675, and 870 nm), although three of them are sufficient for these computations as indicated by Eck et al. (1999). AODs in the above wavelength range have been chosen because AERONET channels in this range of wavelengths are more accurate (Holben et al. 1998; Eck et al. 1999). The AODs at 1020 nm were not taken into account, as the wavelength is affected by the PWV in the entire column of the atmosphere (Kumar et al. 2014). The derivation of AE with respect to $\ln\lambda$ provides the second derivative of AE (α') equals to $-2a_2$ (Eck et al. 1999). α' was derived using observed AOD at 340, 380, 440, 500, 675, and 870 nm wavelengths. Positive α' indicates abundance of fine-mode particles in the size distribution, whereas near zero and negative values of α' indicate a higher amount of coarse-mode particles relative to those of the fine mode (Eck et al. 1999, 2005).

Products obtained by inversion data

Besides the information contained directly in the AOD and its spectral dependence, an inversion algorithm developed by Dubovik and King (2000) and subsequently modified by Dubovik et al. (2002) can be used to retrieve the columnar aerosol characteristics from the direct sun and diffuse sky radiance measurements. Among the retrieved characteristics, there is the vertically averaged aerosol volume size distribution (VSD, $dV(r)/d\ln r$), which is an important parameter in understanding their effect on climate. The aerosol VSDs were retrieved from the sun photometer measurements using 22 radius size bins ranging from 0.05 to 15 μm. The VSD exhibits a bimodal structure, which can be characterized by the sum of two log-normal distributions, as follows:

$$\frac{dV(r)}{d\ln r} = \sum_{i=1}^{2} \frac{C_{v,i}}{\sqrt{2\pi}\sigma_i} \exp\left[\frac{(\ln r - \ln r_{v,i})^2}{2\sigma_i^2}\right] \tag{2}$$

where σ_i is the geometric standard deviation, $r_{v,i}$ is the volume median radius, and $C_{v,i}$ is the volume concentration for fine and coarse modes (Xia et al. 2006, 2016; Alam et al. 2011, 2012; Adesina et al. 2014; Yu et al. 2016b, c).

At each of the four wavelengths, the inversion procedure also provides (i) the SSA; (ii) the scattering phase function, which in turn allows the computation of the ASY; and (iii) the Re and Im parts of the aerosol complex RI. SSA and ASY are crucial inputs for the radiative transfer codes used for the quantification of the aerosol's impact on climate radiative transfer. It is well known that the SSA (ranging from 0 to 1) is the ratio of scattering to the total extinction efficiency, whereas ASY is the cosine-weighted average of the scattering angle for the scattered radiation.

Estimation of DARF and atmospheric heating rate

The DARF at the TOA or the SUR is defined as the difference in the net (down minus up) solar flux (in W m^{-2}) with and without aerosol, i.e.,

$$\Delta F = (F_a\downarrow - F_a\uparrow) - (F_0\downarrow - F_0\uparrow) \qquad (3)$$

where ΔF denotes the DARF (in W m^{-2}) and F_a and F_0 denote the global irradiances with aerosol and without aerosols, respectively, either at the TOA or the SUR. Further, the resultant net atmospheric forcing (ΔF or ATM), also representing the amount of solar energy absorbed by aerosols in the atmosphere, was obtained by the difference between TOA and SUR.

In the present study, we have computed the daily DARF values, within the wavelength range from 0.3 to 4.0 μm (shortwave), using eight radiation streams to obtain the TOA and SUR downward and upward fluxes during clear sky days with and without aerosol separately, and then averaged DARF was estimated for each month during the study period. To accomplish this, we used the standard atmospheric model, SBDART (Ricchiazzi et al. 1998), which uses the discrete ordinates radiative transfer (DISORT) integration of the radiative transfer equations. This model was developed by the atmospheric science community and has been widely used for radiative transfer calculations by several authors (Adesina et al. 2014; Alam et al. 2011, 2012; Tiwari et al. 2015; Srivastava et al. 2015; Yu et al. 2016b, c). Alam et al. (2011) estimated mean DARF for the period 2006–2007 at the TOA of -22 ± 6 W m^{-2} and the SUR of -73 ± 12 W m^{-2} over the megacity Karachi (Pakistan). Similarly, Adesina et al. (2014) reported the averaged DARF at the TOA of -878 ± 3.1 W m^{-2} and the SUR of -25.7 ± 8.1 W m^{-2} over the urban atmosphere of Pretoria during 2012.

Based on the prevailing weather conditions and measured parameters, we set the input in the atmospheric model as "mid-latitude atmosphere (summer and winter)." The crucial input parameters for the estimations of DARF were AOD, AE, SSA, ASY, and surface albedo, taken from the sun-sky radiometer of NUIST site (except the surface albedo). Other input parameters in the model include solar zenith angle, which is calculated using a small code in the SBDART model by specifying a particular date (in terms of Julian day); time (in decimals; UTC); latitude; and longitude. The surface albedo values were obtained from the Ozone Monitoring Instrument (OMI) onboard NASA's Aura satellite through the GIOVANNI online data system, developed and maintained by the NASA GES DISC (http://disc.sci.gsfc.nasa.gov/giovanni).

The atmospheric heating rate (AHR) due to aerosol absorption into the atmosphere (i.e., ΔF or ATM) is calculated from the first law of thermodynamics and hydrostatic equilibrium (Liou 2002) as

$$\frac{\partial T}{\partial t} = \frac{g}{C_p} \times \frac{\Delta F}{\Delta P} \times 24(\text{h/day}) \times 3600(s/\text{h}) \qquad (4)$$

where $\frac{\partial T}{\partial t}$ is the AHR in Kelvin per day (K day^{-1}), $\frac{g}{C_p}$ is the lapse rate where g is the acceleration due to gravity and C_p is the specific heat capacity of air at constant pressure (i.e., 1006 J kg^{-1} K^{-1}), and ΔP is the atmospheric pressure difference between the top and bottom boundaries of the atmosphere (Srivastava et al. 2015; Yu et al. 2016b, c).

Results and discussion

Temporal characteristics of aerosol optical properties

The AOD is representative of airborne aerosol loading in the atmospheric column and is important for the identification of aerosol source regions and evolution. Figure 3 illustrates the time series of daily mean variations in AOD$_{500}$, AE$_{440-870}$, and PWV for the study period observed at a particular site in Nanjing representing cloud-free days. Daily averaged AOD$_{500}$ values show very large day-to-day variations ranging from 0.18 to 3.95, whereas AE$_{440-870}$ varied between 0.22 and 1.57 (Fig. 3a). It is obvious that the pattern of AE followed quite oppositely with AOD suggesting negative correlation between them. During springtime, the high AOD is attributed to large amounts of airborne dust and sand particles (coarse-mode particles) transported from north and northwest of China (e.g., Deng et al. 2012; Li et al. 2015; Han et al. 2015 and references therein), resulting in low AE, whereas AE increases with the increase in AOD during the summer months, which is mainly caused due to abundance of fine-mode particles from anthropogenic activities (biomass burning and urban/industrial). In the case of AOD$_{500}$ and PWV, both AOD and PWV follow a similar pattern (Fig. 3b). PWV ranged between 0.39 and 6.24 cm for the entire study period at the measurement site. Further, PWV and surface RH were higher during the summer resulting in greater aerosol hygroscopic growth and higher aerosol extinction, which is consistent with the results reported by Eck et al. (2005), Kumar et al. (2013), and Wu et al. (2015).

AOD$_{550}$ retrieved from the MODIS sensor on board Terra satellite is also shown in Fig. 3c for the study period over East Asia. As a highly urbanized area with dense population and developed industries, the northern and eastern parts of China (including YRD) were characterized with high aerosol loading (>0.9). On the contrary, lower AOD (<0.1) can be found over the southern part of China (mountainous regions) (Fig. 3c). The present study also attempts to validate the MODIS
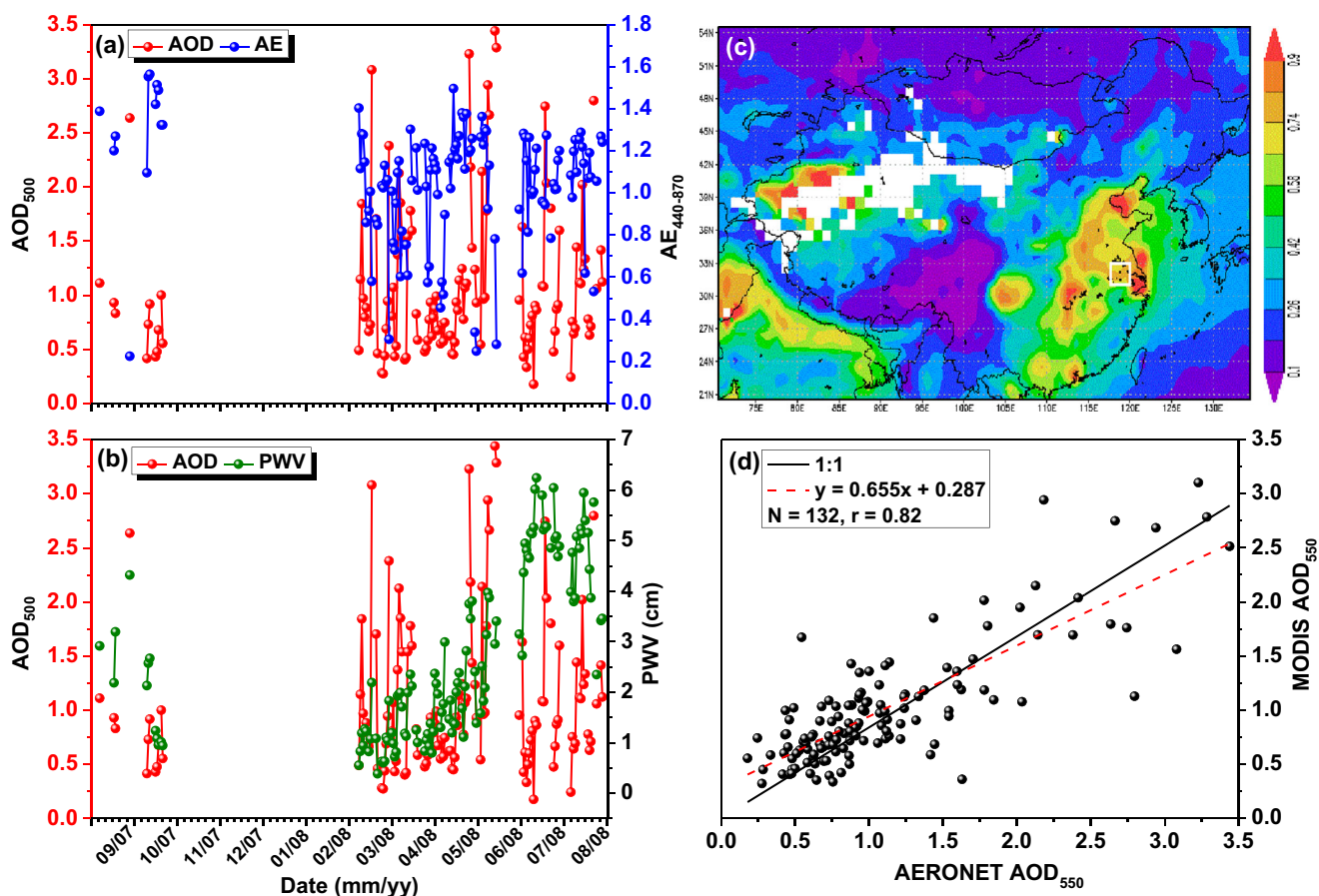
Fig. 3 Time series of daily variations of **a** AOD_{500} versus $AE_{440-870}$, **b** AOD_{500} versus PWV, **c** MODIS AOD_{550} over China, and **d** validation of AOD_{550} between MODIS and AERONET for the study period during September 2007–August 2008. The *solid black line* in **d** corresponds to

1:1 line and the *dashed red line* represents the linear regression fitting to the data points. The correlation coefficients obtained from the regression fitting are also provided. Also shown is the location of Nanjing in **c** represented with a *white color rectangular box*

AOD_{550} over Nanjing in the YRD region. The scatter plot of MODIS AOD_{550} against AERONET AOD_{550} (Fig. 3d) some-what showed good agreement (consistency) between them for simultaneous daily observations with the majority of data points which were concentrated around the 1:1 line. A high correlation coefficient (r) of 0.82 was noticed which indicates that the MODIS can capture the seasonal variability well. The slope (intercept) of the regression fitting was found to be 0.655 (0.287), implying an underestimation of MODIS AOD lower by 35 % compared to AERONET AOD. For more details about the intercomparison between MODIS and AERONET AODs, the readers are advised to refer section S1 and Fig. S1 of the SM. Zhuang et al. (2014) also investigated similar validation of MODIS against AERONET AOD_{550} over Nanjing for the period during January 2011–April 2012, with a fair correlation of $r = 0.76$.

Table 1 presents the monthly and seasonal averaged statistics (calculated from the daily mean values) of different aerosol optical properties and their derived parameters recorded at the measurement location in Nanjing. The interesting feature is noted that there was a distinct seasonal variation of these

parameters. Similar seasonal patterns of AOD, AE, and PWV were reported for the other sites in the YRD and China (Zhuang et al. 2014; Li et al. 2015; Pan et al. 2010; Wu et al. 2015; Wang et al. 2015; Cheng et al. 2015; Che et al. 2015; Xia et al. 2016). The measured AOD_{500} values were found to be higher in summer than those of the other seasons, with the maximum monthly averaged AOD_{500} of 1.62 ± 0.82 in June and the minimum during autumn (October) with the monthly averaged AOD_{500} of 0.62 ± 0.49. The annual mean AOD_{500} during the study period at the experimental station was 0.95 ± 0.41, which is higher ($AOD_{500} \sim 0.78 \pm 0.38$) than that reported by Li et al. (2015) at another place in the same city during 2011–2012. However, AOD in Nanjing is close to some urban sites in China, such as Linan ($AOD_{440} \sim 0.89$) and Taihu ($AOD_{440} \sim 0.86$), and higher than noticed at Beijing ($AOD_{500} \sim 0.77$) and Shanghai ($AOD_{440} \sim 0.75$). This shows that the environmental and climatic effects of aerosols cannot be neglected due to the high aerosol loading over urban Nanjing (Li et al. 2015).

The highest AOD occurred in summer (1.18 ± 0.63), be-cause high temperature and increased RH are beneficial for

Table 1 Statistics of monthly and seasonal averaged aerosol optical properties observed at the measurement station in Nanjing during September 2007–August 2008

Month	AOD_{500}	$AE_{440-870}$	PWV	$EAE_{440-870}$	a_2	α'
September 2007	0.98 ± 0.47	1.13 ± 0.16	2.34 ± 0.94	–	-0.26 ± 0.25	0.51 ± 0.51
October 2007	0.62 ± 0.49	1.05 ± 0.19	1.62 ± 0.66	1.39 ± 0.21	-0.22 ± 0.18	0.43 ± 0.36
March 2008	0.76 ± 0.50	1.08 ± 0.18	0.92 ± 0.33	1.14 ± 0.14	-0.01 ± 0.31	0.02 ± 0.62
April 2008	0.82 ± 0.48	0.95 ± 0.26	1.20 ± 0.45	1.01 ± 0.26	$+0.03 \pm 0.25$	-0.06 ± 0.51
May 2008	0.92 ± 0.40	1.02 ± 0.36	2.05 ± 0.72	1.03 ± 0.37	-0.03 ± 0.25	0.06 ± 0.50
Jun 2008	1.62 ± 0.82	1.25 ± 0.17	3.41 ± 0.71	1.28 ± 0.03	-0.34 ± 0.28	0.67 ± 0.56
July 2008	0.85 ± 0.51	1.10 ± 0.20	5.02 ± 0.42	1.11 ± 0.29	-0.17 ± 0.34	0.33 ± 0.67
August 2008	1.05 ± 0.57	1.17 ± 0.17	4.31 ± 0.82	1.22 ± 0.08	-0.35 ± 0.27	0.70 ± 0.54
Autumn	0.80 ± 0.48	1.09 ± 0.17	1.98 ± 0.80	1.39 ± 0.21	-0.24 ± 0.22	0.47 ± 0.44
Spring	0.83 ± 0.46	1.02 ± 0.27	1.39 ± 0.50	1.06 ± 0.26	-0.01 ± 0.27	0.01 ± 0.54
Summer	1.18 ± 0.63	1.19 ± 0.18	4.25 ± 0.65	1.21 ± 0.13	-0.29 ± 0.30	0.57 ± 0.59
Mean	0.95 ± 0.41	1.10 ± 0.21	2.61 ± 0.68	1.17 ± 0.18	-0.17 ± 0.16	0.34 ± 0.30

the formation and hygroscopic growth of fine-mode aerosols. In addition, stronger atmospheric convection enhances the vertical transportation of particles near the surface in summer. Also, the higher temperature during summer favors the photochemical processes leading to production of secondary aerosols, mostly from anthropogenic origin (e.g., Cheng et al. 2015; Xia et al. 2016). Although there was a stronger wet removal of aerosols (maximum precipitation, see Fig. 2), the static atmospheric condition, aerosol hygroscopic growth, secondary aerosol formation, and biomass burning pollutants from surrounding agricultural areas cause more aerosol accumulation and then enhance AOD in summer (Xia et al. 2013). High AODs in spring (0.83 ± 0.46) are likely associated with pollutant pooling in low atmospheric layers by stagnant meteorological conditions, stronger surface winds, local sand dust emissions, and some transported desert dust coarse particles from the north and northwest of China to the observational site (Xia et al. 2006, 2013; Cheng et al. 2015; Li et al. 2015; Yu et al. 2016a, c). This coincides well with the low value in $AE_{440-870}$ (1.02 ± 0.27) resulting in a higher contribution of coarse-mode particles. Sometimes, the decrease in AOD during the spring might be a consequent result of cloud scavenging, high wind speed, and low atmospheric PWV conditions. These conditions would also lead to weak generation mechanisms and a remote chance of hygroscopic growth of aerosols (Cheng et al. 2015). During autumn, the dispersal of pollutants at Nanjing is easily accelerated because of increased velocity of winds, which leads to a smaller AOD. AOD in September (0.98 ± 0.47) was found to be higher than in other months of autumn and spring which can be influenced by burning of agricultural residues after harvest (Xia et al. 2013), resulting in maximum AE value (1.13 ± 0.16) with the dominance of fine-mode aerosols.

In general, similar seasonal variations of AOD have been investigated by several previous authors leading to frequent haze-fog conditions in the recent years (Xia et al. 2013; Cheng et al. 2015; Li et al. 2015; Wu et al. 2015). Alam et al. (2011) reported a high AOD_{500} value of 0.92 ± 0.28 in Karachi, Pakistan (Asia), during summer (July) of 2006–2007, which could be attributed to the fact that it is a large urban-industrial and coastal city. The maximum AOD_{440} values of 0.60 ± 0.23 and 0.47 ± 0.24 were noticed in October (biomass burning season) and April (desert dust), respectively, as investigated by El-Metwally et al. (2011) from the sun photometer measurements performed in Cairo, Egypt (Africa), between October 2004 and March 2006. Similarly, Esteve et al. (2014) also found that the AOD at 500 nm presents maximum values in summer (0.28 ± 0.01 in July) and minimum values in winter (0.080 ± 0.004 in December), with a mean value of 0.193 ± 0.004 at Burjassot, Spain (Europe), during the period 2003–2011. Also, Adesina et al. (2014) examined the mean AOD_{500} which exhibited two maxima that occurred in summer (February) and winter (August) having values of 0.36 ± 0.19 and 0.25 ± 0.14, respectively, over an urban site, Pretoria, in South Africa (Africa) with the data collected from a sun photometer for a 1-year period (January–December 2012). Further, Brock et al. (2015) reported a low mean value of AOD at 532 nm which is 0.19 at Atlanta, Georgia (USA), during 2011–2014 using AERONET's sun photometer retrieved data. Recently, a clear seasonal pattern was observed in the work of Romero et al. (2016) with summer (0.23 ± 0.12) values being clearly higher than the winter values (0.08 ± 0.01) derived from multifilter rotating shadowing radiometer (MFRSR) observations carried out at Girona, Spain (Europe), from June 2012 to June 2014.

AE is a measure of the relative dominance of fine-mode aerosols over the coarse-mode aerosols (Kumar et al. 2013; Adesina et al. 2014; Xia et al. 2013; Wang et al. 2015 and references therein). The mean and standard deviation of $AE_{440-870}$ for the studied period were measured as 1.09 ± 0.17, 1.02 ± 0.27, and 1.19 ± 0.18 during the autumn, spring, and summer seasons, respectively. The monthly mean values

of AE varied widely, representing a minimum value of 0.95 ± 0.26 in April and maximum (1.25 ± 0.17) in June. Most of the monthly mean values of AE were higher than 1 (see Table 1) during the study period, indicating that the aerosol particle size at the measurement site is dominated with fine-relative to coarse-mode particles (Xia et al. 2013; Cheng et al. 2015; Yu et al. 2016c). High AE values in summer and autumn seasons indicate a more abundance of fine-mode aerosols, while low AE ones in spring reflect the large contribution of coarse-mode particles (see Table 1). The anthropogenic fine-mode aerosols in summer are mostly carbonaceous and sulfate aerosols generated from biomass burning and urban/industrial activities, in addition to those from gas-to-particle conversion mechanisms (El-Metwally et al. 2011), whereas the dominance of coarse-mode aerosols during spring is mainly from sea salt and mineral dust (Wu et al. 2015). But it is clear from the table that April is the month with the most occurrences of dust storm events in Nanjing and other sites in China, and is probably the month with the long-range transport of dust particles from north (Mongolian Desert) and northwest (Taklimakan Desert) of China (Li et al. 2015). These unusual dust outbreaks during the spring months in Nanjing were also reported by Pan et al. (2010), Zhuang et al. (2014), and Han et al. (2015). Furthermore, similar major dust episodes in springtime were recently observed in several urban areas of China (Wang et al. 2015; Cheng et al. 2015; Yu et al. 2016b, c).

The PWV values varied in the range from 0.92 to 5.02 cm, with maximum peak in the month of July (5.02 ± 0.42 cm) and minimum value during March (0.92 ± 0.33 cm) (Table 1). Further, it was noticed to be 1.98 ± 0.80 cm during autumn, 1.39 ± 0.50 cm during spring, and 4.25 ± 0.65 cm during summer, respectively, with an annual mean of 2.61 ± 0.68 cm for the entire study period at the observation station. It was found that the maximum PWV in summer is approximately 2–5 times larger than that in other seasons. The spectral curvature a_2 obtained through the second-order polynomial fit in the spectral range 340–870 nm is also analyzed during the study period. The monthly variation of a_2 permits an assessment about the dominance of fine- ($a_2 < 0$) or coarse-mode ($a_2 > 0$) aerosols (Eck et al. 1999; Kumar et al. 2013 and references therein) for each month in Nanjing. It is clearly depicted from Table 1 that the negative a_2 values were observed in all the months, except for April, indicating abundance of fine-mode aerosols throughout the study period. It can be further stated that large AOD and AE associated with large negative a_2 correspond to fresh smoke aerosols from any kind of biomass burning (Eck et al. 2005). The positive curvature in the month of April indicates dominance of coarse-mode particles, which coincides with the low AE. The values of the second derivative of AE (α') computed from the polynomial fit to the AOD in the range 340–870 nm are also presented in Table 1. In the present study, α' observed to be positive in all the months,

except for April (approaching zero or negative), shows the abundance of fine-mode aerosols attributed from anthropogenic activities, whereas negative α' values were mainly associated with coarse-mode (dust and sand particles) aerosols. The maximum of α' (large positive) in summer also proves the presence of fine-mode aerosols due to their hygroscopic nature with increased atmospheric PWV.

Identification and classification of aerosol types

Aerosols are classified into different types based on their abundance as expressed via AOD, aerosol particle size, and absorption. AOD versus AE and/or absorption AE (AAE) versus extinction AE (EAE) techniques are commonly used for the identification of the different aerosol types (Kaskaoutis et al. 2009; Alam et al. 2011; Giles et al. 2012; Kumar et al. 2014, 2015; Xia et al. 2016; Yu et al. 2016b). Better characterization of aerosol properties can be done using scatter plots of AOD_{500} versus $AE_{440-870}$ as both are functions of wavelength (also between $AAE_{440-870}$ and $EAE_{440-870}$) from which different aerosol types can be obtained for a specific location through determination of physically interpretable cluster regions of the diagram (Pace et al. 2006). More details about the threshold limits applied for the identification of aerosol types are discussed in Table S2 of the SM. The scatter diagram between AOD_{500} and $AE_{440-870}$ for the study period over Nanjing is demonstrated in Fig. 4a. The threshold values of continent clean (CC) and marine (MA) aerosol types are taken as AOD <0.3; AE >1.0 and AOD <0.3; AE <0.9, respectively, having a very small amount of points in their cluster regions. But a very large amount of points were accumulated in the cluster region AOD >0.6 and AE >1.0, which corresponds to the particles of biomass burning and urban-industrial (BB/UI) aerosol type. Similarly, a moderate number of points was concentrated in the region with higher AOD (>0.7) and AE <0.7, indicating the presence of desert dust (DD) aerosol type. The remaining scattered points corresponding to a wide range of AOD and AE values which do not fall in any of the above categories were characterized as the mixed (undetermined) (MX) aerosols (Pace et al. 2006) due to the external or internal mixture of anthropogenic and natural aerosols. During the study period, BB/UI (45.75 %) was the dominant aerosol type followed by the MX (42.35 %) aerosol type, with a minor contribution from MA (0.53 %) and CC (3.48 %) types of aerosols. The vast majority of the cases with high AOD (>0.6) were associated with high AE (>1.0) values and, therefore, with the presence of BB/UI aerosols. The increase in AE with increasing AOD indicates the presence of fine-mode aerosol in the atmospheric column. Few cases of extremely large AOD (>1.0) values were accompanied with low AE (<0.7) values, indicating the dominance of coarse-mode aerosols of DD type transported from the deserts in the north and northwest of China (Li et al. 2015; Cheng et al. 2015). Kumar
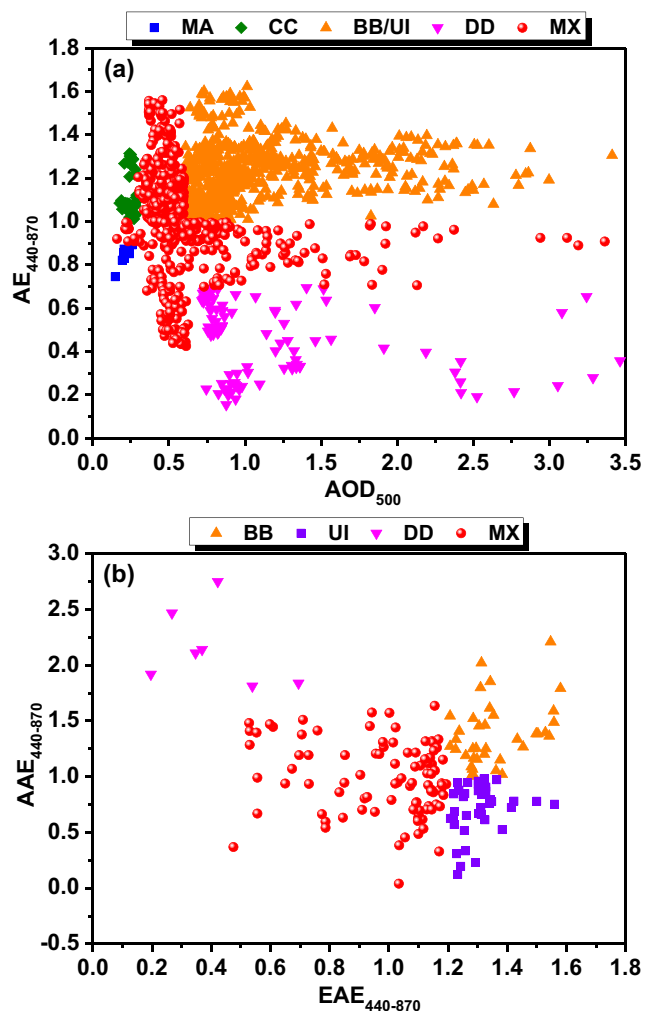
Fig. 4 Scatter plot of **a** AOD$_{500}$ versus AE$_{440–870}$ and **b** EAE$_{440–870}$ versus AAE$_{440–870}$ with the instantaneous data points identifying dominant aerosol types during the study period at Nanjing. *MA* marine aerosol, *CC* continental clean, *BB/UI* biomass burning/urban-industrial, *DD* desert dust, *MX* mixed

et al. (2014) and Che et al. (2014) also reported the dominance of small particles representing BB/UI aerosol type over Beijing (January 2013) and Mpumalanga (2005-2006) from sun photometer measurements.

Recently, Giles et al. (2012) suggested that the relationship between AAE and EAE can be used to further categorize the dominant aerosol type or optical mixture from AERONET retrievals. Figure 4b shows a scatter plot of AAE$_{440–870}$ versus EAE$_{440–870}$ observed at Nanjing during the study period. The DD type aerosol was characterized by EAE <0.7 and AAE >1.5. The EAE >1.2 associated with AAE >1.0 represents the BB aerosol type. Further, the UI category aerosol types for the relationship between EAE and AAE were analyzed with EAE >1.2 and AAE <1.0. It is obvious from Fig. 4b that the dominant aerosol types can be classified as MX category followed by BB and UI categories with the DD type being

the least. The MX category occurrence was about 46.33 %, while the BB, UI, and DD were about 20.78, 28.65, and 3.90 %, respectively. Russell et al. (2010) investigated that the AAE values are close to 1 for black carbon, higher for biomass burning aerosols, and highest for Saharan dust aerosols. Similar observations have been reported by Alam et al. (2012), Che et al. (2014, 2015), and Yu et al. (2016b) over Karachi, Shenyang, and Beijing, respectively. The dominant aerosol type at Kunming in China is BB and UI aerosol as noticed by Zhu et al. (2016). Recently, Che et al. (2014) and Yu et al. (2016b) also found the abundance of MX followed by UI and BB aerosol types at Beijing in January 2013. More research is therefore required into improving the remote identification of aerosol types, which are undetermined (Russell et al. 2010).

The spectral variation of AE can provide further information about the aerosol particle size and distribution. Gobbi et al. (2007) proposed a simple graphical method and used it to track mixtures of aerosol pollution with mineral dust, to distinguish aerosol growth from cloud contamination and to observe aerosol humidification. The method proposed by Gobbi et al. (2007) has been utilized by several authors and applied to different environments (e.g., Kumar et al. 2014; Li et al. 2015; Cheng et al. 2015; Che et al. 2015). The curves/ lines (black and cyan) related to the graphical scheme have been drawn using the Mie theory with a refractive index $m = 1.4$–0.001i. Figure 5 presents the classification of aerosol properties as a function of AE$_{440–870}$ and the difference of AE (dAE = AE$_{440–675}$ − AE$_{675–870}$) for bimodal and log-normal size distributions. Different colors of closed circles in Fig. 5
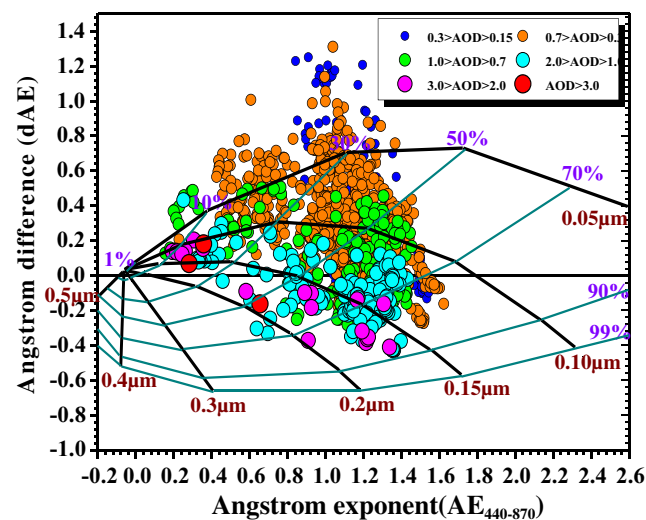

Fig. 5 Ångström exponent difference, dAE = AE (440–675 nm) − AE (675–870 nm), as a function of AE (440–870 nm) and AOD$_{675}$ (color-sized scale) over Nanjing, for bimodal and log-normal size distribution. The *black lines* indicate the fixed effective radius (R_f) of the fine mode and the *dark cyan lines* for a fixed fraction (η) of fine mode to the AOD at 675 nm. Increase of the *circle symbols* denotes increase in AOD

represent the values of AOD_{675} with the increase in circle size indicating an increase in aerosol concentration. Only cloud-screened data with AOD_{675} >0.15 are used in the study. The black lines are for a fixed size of the fine-mode effective radius (R_f) and the cyan lines are for a fixed fraction (η) contribution of fine mode to the AOD at 675 nm.

Several key features are obvious from Fig. 5. It is seen that some of the data points at low AOD values do fall outside the classification scheme and these may be associated with larger errors in AE, dAE estimation, and uncertainties while measuring AOD_{675}. The scatter plot shows that high AOD (>1.0) values were mainly clustering at high AE (>1.0) which were associated with fine-mode aerosol with dAE <0 and large η > 70 % (R_f< 0.12 μm) value. However, we noticed few cases associated with low AOD (<0.3), AE <0.7 and high R_f >0.2 μm and several cases where moderate-to-high AODs (>1.0) were associated with low AE (<1.0) and η <30 % values suggesting the presence of coarse-mode particles. This pattern is similar to that of the classification noticed at Mpumalanga (Kumar et al. 2014), Shenyang (Che et al. 2015), Nanjing (Li et al. 2015), and Shanghai (Cheng et al. 2015). The main feature revealed from the figure is that increasing AOD is associated with an increase of fraction (η) contributing fine-mode aerosols with negligible variation of AE and slight increase in fine-mode fraction. This means that increasing AOD is strongly associated with the presence of more fine-mode aerosols (so the decrease in dAE from positive to negative) and with only a slight increase in fine-mode radius (representing aging processes in the atmosphere). The main finding is the contribution of more fine-mode aerosols, which, however, do not influence the AE but only the fine-mode fraction. The influence of dust was observed in the case of the highest AOD, on which the AE is much lower and the dAE becomes positive.

Curvature effect on AOD and AE

To get further information about the nature of aerosol size distribution, coefficients a_1 and a_2 obtained through second-order polynomial fit (using Eq. 1) are analyzed for all the seasons (except for winter). Coefficients a_2 and a_1 exhibit a wide range of values showing strong seasonal variation. From Fig. 6a, it is clear that the low AOD_{500} (<0.3) was found to associate with wide variability in a_2 values (both positive and negative), mostly implying a positive curvature. In contrast for high AOD_{500}, a_2 tends to zero or negative indicating a negative curvature. In the case of AE, the large positive a_2 values that can be clearly identified for low AE (<1.0) (Fig. 6d) indicate the presence of desert dust coarse particles. Coefficient a_2 values exhibit strong negative values with the dominance of fine aerosols attributed to biomass burning and urban/industrial for high AE values (>1.0).

Also, Schuster et al. (2006) showed that the relation a_2–$a_1 = \alpha$ can be considered valid for a bimodal aerosol size

distribution. Under such conditions, a_2–$a_1 \geq 2$ represents AOD spectra dominated by fine-mode aerosols, while a_2–$a_1 \leq 1$ represents AOD spectra dominated by coarse-mode aerosols. AOD spectra with a_2–a_1 value between 1 and 2 represent a wide range of fine-mode fractions and/or mixture of modes (see Table S2 of the SM). From Fig. 6b, it is revealed that the station was characterized by the dominance of a wide range of fine-mode fractions or mixture of modes as a_2–a_1 values lie between 1 and 2 over Nanjing during the study period. It is notable that 23, 16, and 4 % of AOD spectra have a_2–$a_1 \leq 1$ indicating the presence of coarse-mode aerosols during the spring, summer, and autumn seasons, respectively. Thus, the results indicate the dominance of fine-mode aerosol particles relative to coarse-mode at Nanjing during the study period. A strong correlation was observed between a_2–a_1 and AE during all seasons with the correlation coefficient varying between 0.98 and 0.99. Similar results were also noted from the other studies by Kumar et al. (2013, 2014) and Kedia et al. (2014) and pointed out the validity of a_2–$a_1 = \alpha$.

Figure 6c shows the scatter plot between AOD_{500} and α' for each season during the period of study at a particular site in Nanjing. The majority of α' values were positive when AOD >1.0 (high AE, Fig. 6f), suggesting the increased contribution of fine-mode particles to the aerosol size distribution relative to coarse mode. For small AOD_{500}, there is a large range of values both negative and positive (from −2 to +2). This is an indication of the existence of bimodal aerosol size distribution at relatively lower AODs, with dominance of fine- and coarse-mode particles (Eck et al. 1999; Schuster et al. 2006). A similar relationship for AOD versus α' has been observed by several authors (Eck et al. 1999; Kedia et al. 2014; Kumar et al. 2013 and references therein) for different aerosol types.

Seasonal variations of intensive aerosol properties

Spectral AOD showed a pronounced seasonal variation, with maximum values in summer followed by spring and minimum in autumn season (Fig. 7a). It is obviously evident from Fig. 7a that the AOD occurring during spring and autumn seasons looks comparable. Similar seasonal variation was observed at many other sites over the YRD region including Nanjing (Zhuang et al. 2014; Li et al. 2015), Shanghai (Cheng et al. 2015), over north China, including Beijing (Xia et al. 2006; Che et al. 2014), Xianghe (Li et al. 2015) and Shenyang (Che et al. 2015), and Longfengshan (Wang et al. 2010) in northeast China. Kim et al. (2010) also demonstrated a similar seasonal variation of AOD over eastern Asia, determined from multiyear MODIS, LIDAR, and AERONET radiometer measurements.
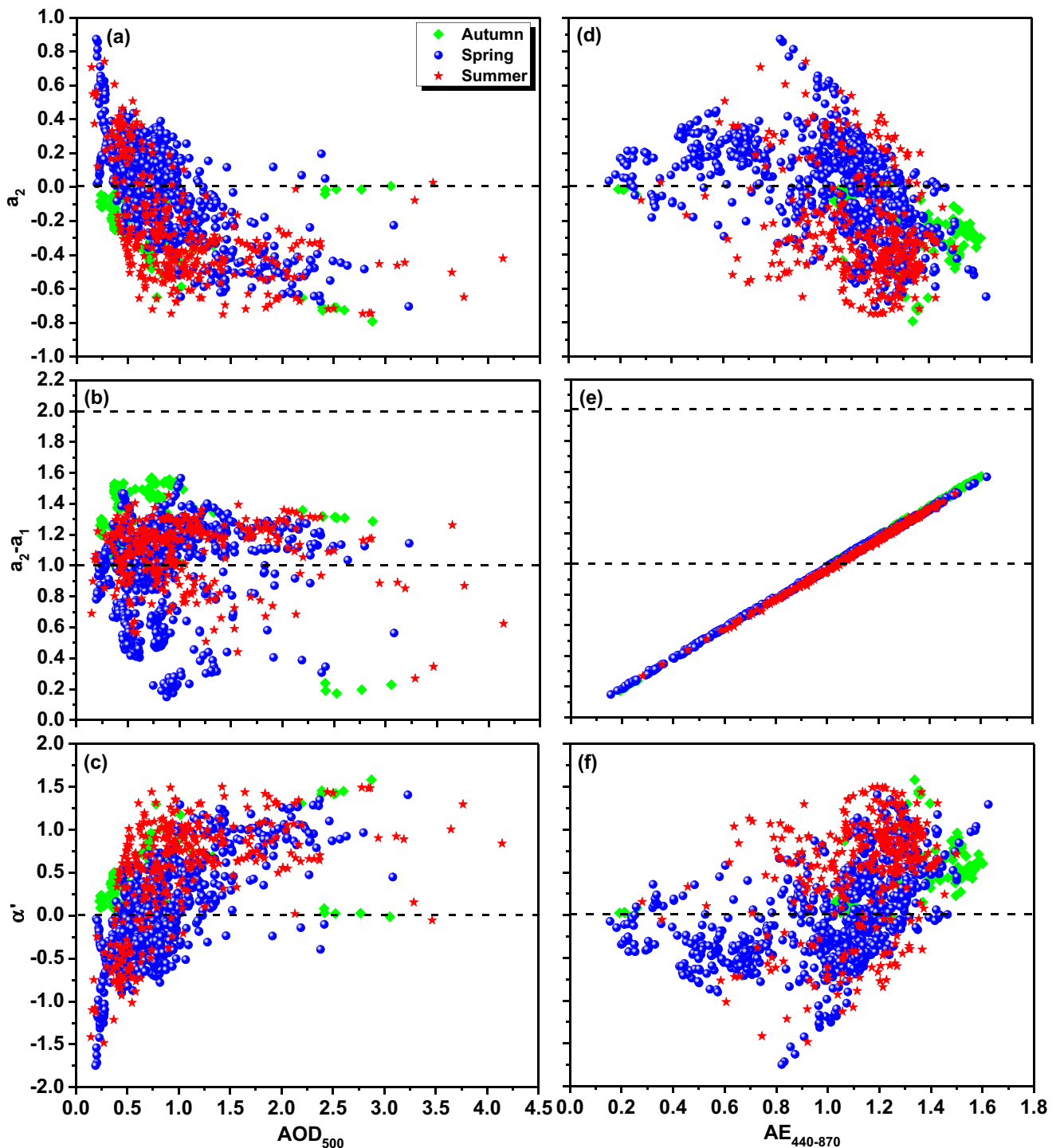
Fig. 6 Seasonal scatter plots (except for winter) between the curvature a_2, difference of polynomial coefficients a_1 and a_2 ($a_2 - a_1$), and derivative of AE (α') versus AOD_{500} (**a–c**) and $AE_{440–870}$ (**d–f**) for the study period observed over Nanjing

The retrieved size distributions were averaged by season and showed obvious variation. It is evident from Fig. 7b that the VSD showed a bimodal pattern with fine-mode peak at about 0.15 μm (except in summer which is about 0.2 μm) and a radius of ~3.5 μm for the coarse-mode peaks (except in spring about 3.0 μm with a

maximum volume concentration of 0.12 μm³). The size distributions in the coarse mode were higher in spring (increased by 40–70 %) and lower in the summer season. The higher values of volume concentration in spring compared to the other seasons were due to the long-range dust transportation from remote source locations and locally
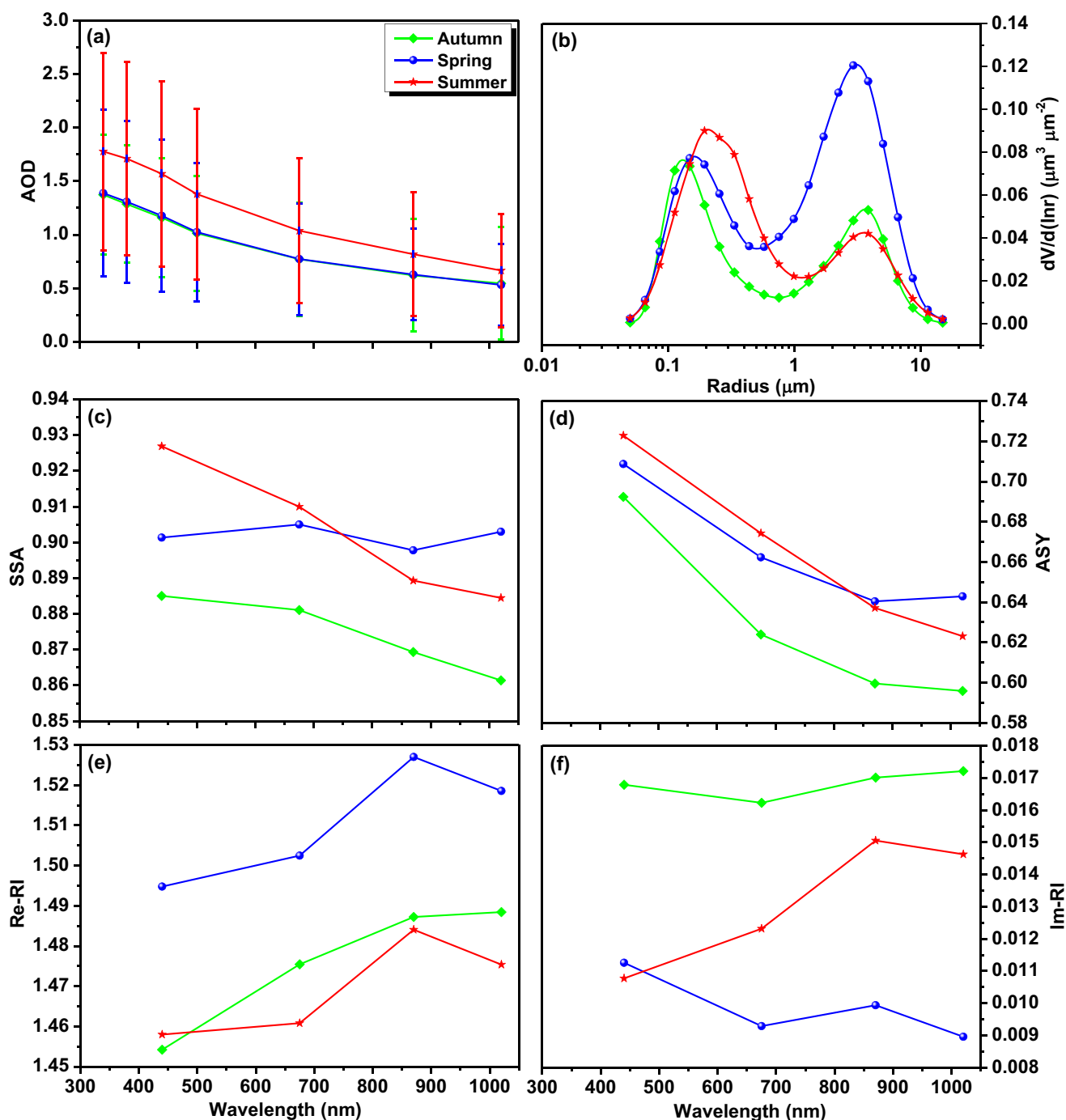
Fig. 7 Seasonal spectral variations of **a** AOD, **b** volume size distribution, **c** SSA, **d** asymmetry parameter, **e** real, and **f** imaginary parts of the complex refractive index during the study period at the measurement site

generated sand dust particles (Xia et al. 2013; Wu et al. 2015). The highest volume concentration in the fine mode was noticed during the summer season and is due to more anthropogenic activities (biomass burning and urban-industrial activities), resulting in a higher AOD (Wu et al. 2015; Cheng et al. 2015 and references therein). Several earlier researchers also found similar seasonal variations in VSDs using AERONET measurements

(e.g., El-Metwally et al. 2011; Adesina et al. 2014; Wu et al. 2015; Cheng et al. 2015; Yu et al. 2016b, c).

SSA exhibits different spectral behavior for different types of aerosol: increasing with wavelength for DD aerosols and decreasing with wavelength for BB/UI aerosols (Dubovik et al. 2002). Table 2 presents the monthly averaged SSA and ASY values with corresponding standard deviations retrieved at four wavelengths of 440, 675, 870,

Table 2 Monthly mean values of spectral SSA and ASY with corresponding standard deviations for the mean during the study period

Month	Single scattering albedo (SSA)				Asymmetry parameter (ASY)			
	440 nm	675 nm	870 nm	1020 nm	440 nm	675 nm	870 nm	1020 nm
October 2007	0.88±0.04	0.88±0.07	0.87±0.08	0.86±0.09	0.69±0.02	0.62±0.03	0.60±0.02	0.59±0.02
March 2008	0.90±0.03	0.89±0.04	0.88±0.04	0.89±0.05	0.70±0.02	0.65±0.03	0.63±0.02	0.64±0.02
April 2008	0.90±0.03	0.91±0.03	0.91±0.03	0.91±0.03	0.71±0.02	0.67±0.03	0.64±0.03	0.65±0.03
May 2008	0.90±0.02	0.91±0.04	0.90±0.05	0.91±0.05	0.71±0.03	0.67±0.04	0.64±0.04	0.64±0.04
June 2008	0.92±0.04	0.90±0.06	0.88±0.06	0.89±0.06	0.70±0.03	0.65±0.03	0.62±0.02	0.62±0.01
July 2008	0.93±0.04	0.91±0.05	0.89±0.06	0.88±0.07	0.73±0.04	0.68±0.05	0.65±0.04	0.63±0.04
August 2008	0.93±0.04	0.91±0.06	0.89±0.08	0.88±0.08	0.74±0.03	0.68±0.02	0.64±0.02	0.62±0.02

and 1020 nm. It is clear from the table that SSA and ASY are wavelength dependent. SSA shows an increasing trend with wavelength in April and May due to the influence of dust activities, which are highly scattering in nature (Xia et al. 2006, 2013; Cheng et al. 2015; Wang et al. 2015; Yu et al. 2016c). Overall, the SSA values at lower wavelength (440 nm) were lower in October and higher in June and July. Singh et al. (2004) also found that the SSA values increased during summer, attributed to hygroscopic growth of water-soluble aerosols in the presence of high PWV and long-range transport of dust aerosols. Recently, Yu et al. (2016c) also reported that the SSA increased with wavelength on dust days selected during 2001–2014 over urban Beijing, indicating the presence of more scattering coarse particles.

Figure 7c exhibits spectral variations of SSA during all the seasons, except for winter measured at the measurement site in Nanjing. We observed a reasonable dependence of SSA with wavelength in all the seasons such that SSA decreases with wavelength, except for spring, but Re-RI increases with wavelengths in all seasons (Fig. 7e). The decreases in SSA with increase in wavelength can be attributed to the dominance of absorbing type of BB/UI aerosols in Nanjing. This is because lower SSA at longer wavelengths is obtained due to minimum probability for interaction between solar radiation and absorbing aerosols (Singh et al. 2004). The increase in SSA with wavelength is a fingerprint of dust due to higher absorption at longer wavelengths (in the UV band). The same is observed in the case of Im-RI (Fig. 7f), which contains information about the absorption properties of aerosols, where the Re-RI part defines the scattering. The readers are advised to refer section S2 of the SM for more details about the Re-RI and Im-RI observed at Nanjing during the study period. Both panels c and f of Fig. 7 verify the dominance of scattering aerosols during spring (Yu et al. 2016c). Several earlier researchers (e.g., Xia et al. 2006; Wu et al. 2015; Cheng et al. 2015) found a similar trend of decreasing SSA with increase in wavelength during all seasons, except in spring. The magnitude of ASY was found to decrease with increasing wavelength during all the seasons (Fig. 7d). However, an increase in ASY was observed in the near-IR region (1020 nm) during spring, attributed to the presence of dust particles having larger size.

Estimation of DARF and AFE from the SBDART model

The monthly evolution of the averaged values of DARF at the TOA and the SUR obtained at the observation station in Nanjing during September 2007–August 2008 is shown in Fig. 8a. The summary of inputs used in the computation of DARF from the SBDART model for the selected days during the study period is listed in Table 3 and the output fluxes generated are presented in Table S3 of the SM. The DARF at the SUR showed a strong variability during the study period, although the variability at the TOA is only slight, presenting maximum values in June (-133 W m^{-2}) and July (-136 W m^{-2}) of 2008 and minimum values in October 2007 (-75 W m^{-2}). The monthly DARF at the TOA varied from -22 to -34 W m^{-2}, with a mean value of -29.5 ± 3.8 W m^{-2}, and that at the SUR, it ranged from -75 to -136 W m^{-2}, with a mean value of -112 ± 20.8 W m^{-2}. The negative values at the SUR indicate a decrease of the solar radiation reaching the ground, which produces cooling of the Earth's surface, while at the TOA, they indicate an increase of the light that is scattered back to space, cooling the Earth-atmosphere system. The mean DARF obtained at a site in Nanjing was more or less comparable with that obtained by Wu et al. (2015) over Tongyu at the TOA and Alam et al. (2011) for Karachi at the SUR and was slightly higher/lower than the values obtained at other sites in the world by several investigators (see Table 4). Valenzuela et al. (2012) computed the monthly mean values of DARF during the desert dust events, which ranged from -13 ± 8 to -34 ± 15 W m^{-2} at the SUR and from -4 ± 3 to -13 ± 7 W m^{-2} at the TOA over Granada (southeastern Spain) during 2005–2010. Similarly, Esteve et al. (2014) investigated the mean values of DARF at the TOA and the SUR of -2.2 ± 1.3 and -17 ± 10 W m^{-2}, respectively, in Burjassot, Spain, an urban coastal site on the
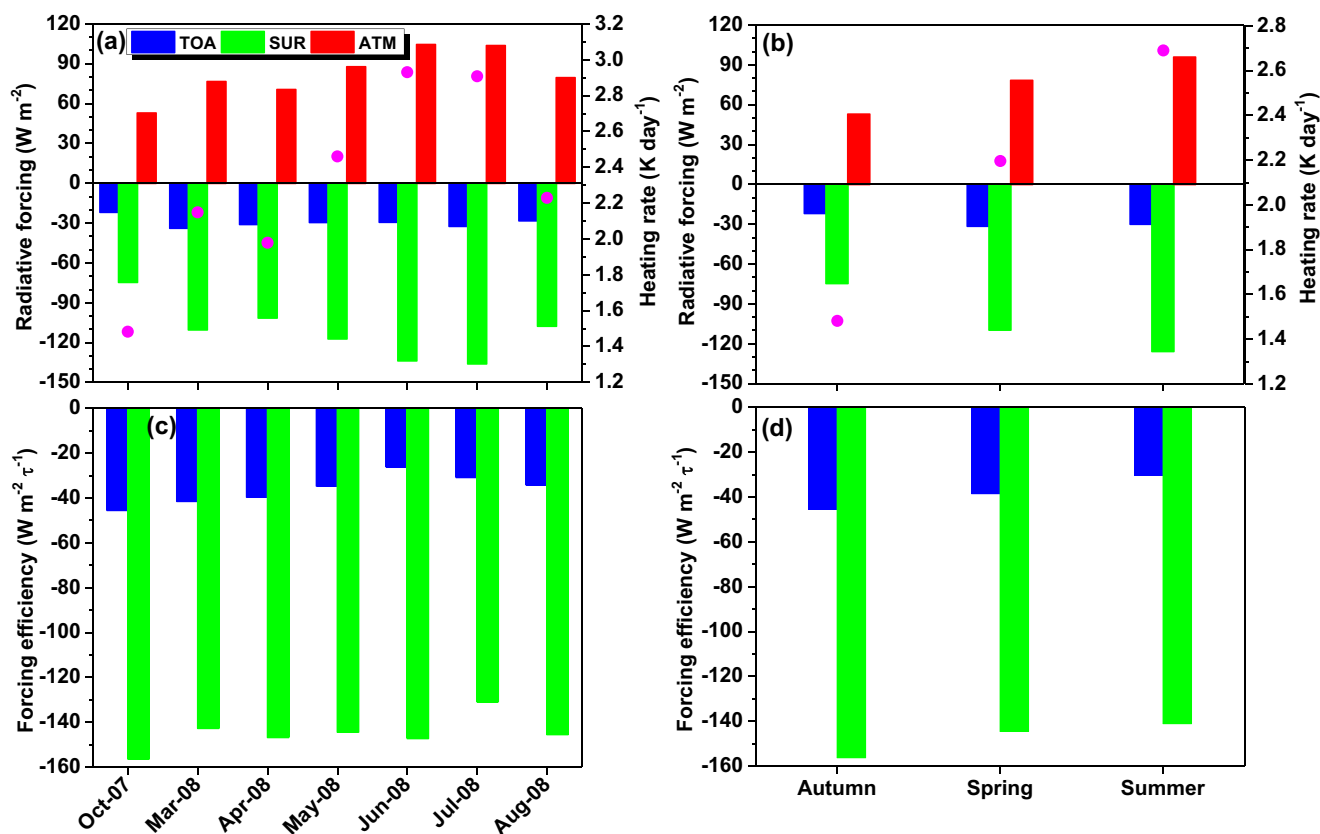
Fig. 8 Monthly and seasonal evolutions of **a**, **b** direct aerosol radiative forcing and **c**, **d** aerosol forcing efficiency estimated at the top of atmosphere (TOA), the surface (SUR), and within the atmosphere (ATM) along with the corresponding AHR values (with *solid circles* indicated in *magenta color*) estimated at the measurement site in Nanjing during the study period

western Mediterranean for the period 2003–2011. Recently, Yu et al. (2016c) found that the shortwave DARF values ranged between −166.6 and −236.1 W m^{-2} at the SUR and between −65.8 and −115.6 W m^{-2} at the TOA over Beijing for the major dust storm events observed during 2001–2014.

Table 3 Summary of inputs used in the SBDART model to estimate DARF (TOA and SUR) for the selected days. The corresponding output results generated from the model are provided in Table S3 of the SM

Date: 19 March 2008; Julian day, 79; decimal time (UTC), 6.25; surface albedo = 0.15

Input	440 nm	675 nm	870 nm	1020 nm
AOD	2.039	1.374	1.047	0.852
SSA	0.962	0.967	0.970	0.972
ASY	0.740	0.713	0.691	0.685
AE$_{440–870}$	0.981			

Date: 10 April 2008; Julian day, 101; decimal time (UTC), 1.48; surface albedo = 0.27

AOD	0.466	0.313	0.284	0.244
SSA	0.894	0.907	0.882	0.892
ASY	0.719	0.685	0.662	0.674
AE$_{440–870}$	0.774			

The monthly variations of DARF in the ATM and the corresponding estimated AHR are also shown in Fig. 8a. The ATM forcing variations were found to be varying from +53 to +104 W m^{-2}, with a mean value of +82.1 ± 18.3 W m^{-2}. This suggests a significant absorption of solar radiation by the atmosphere, which produces a net warming effect within the atmosphere. The corresponding AHR varied between 1.48 and 2.93 K day^{-1}, with a mean value of 2.31 ± 0.52 K day^{-1} during the period of study at a particular site in Nanjing. Similar to the SUR forcing, significantly large values of ATM forcing and corresponding AHR were observed during May–July 2008. This suggests a relatively large abundance of absorbing aerosols with higher AOD and lower SSA values over the station, as also observed by other investigators (Singh et al. 2004; Alam et al. 2011, 2012; Valenzuela et al. 2012; Esteve et al. 2014; Srivastava et al. 2015; Tiwari et al. 2015 and references therein). It is also revealed from Table 5 that the comparison of TOA and SUR forcing retrieved from the AERONET and SBDART showed good agreement. Overall, the SUR forcing is high for AERONET than SBDART and the TOA forcing is almost comparable for AERONET and SBDART. The correlation coefficients during the entire period of observation between AERONET and SBDART at the SUR and the TOA are 0.98 and 0.97, respectively (Fig. 9a).

Table 4 Comparison of direct aerosol radiative forcing (in W m^{-2}) at the TOA and the SUR derived from the present study with that of the previous studies

Site	Country	Study period	SUR	TOA	Reference
Nanjing	China	2007–2008	−75 to −136	−22 to −34	Present study
Nanjing	China	2011–2012	−32.4	−10.9	Zhuang et al. (2014)
Tongyu	China	2010–2014	−75	−29	Wu et al. (2015)
Dibrugarh	India	2010–2014	−27	−6	Pathak et al. (2015)
Manora Peak	India	2006–2008	−3 to −50	−2 to +14	Srivastava et al. (2015)
Kanpur	India	2001–2010	−42 to −57	−12 to −18	Kaskaoutis et al. (2013)
Hyderabad	India	2008–2009	−65 to −80	−17 to −23	Sinha et al. (2013)
Bangalore	India	2004–2005	−20 to −42	+2 to +5	Satheesh et al. (2010)
Ahmedabad	India	2006–2008	−31 to −41	−4 to −12	Ramachandran and Kedia (2012)
Gosan	Korea	2001–2008	−27	−16	Kim et al. (2010)
Cairo	Egypt	2004–2006	−46 to −81	−15 to −25	El-Metwally et al. (2011)
Karachi	Pakistan	2006–2007	−56 to −99	−7 to −35	Alam et al. (2011)
Burjassot	Spain	2003–2011	−6 to −29	−2 to −4	Esteve et al. (2014)
Granada	Spain	2005–2010	−21 ± 9	−7 ± 5	Valenzuela et al. (2012)
Toulon	France	2005–2006	−61.8 to −64	−7.7 to −9.8	Saha et al. (2008)
Lampedusa	Italy	2010	−69.9 ± 3.4	–	Di Sarra et al. (2011)
Pretoria	South Africa	2012	−15 to −39	−7 to −18	Adesina et al. (2014)

Seasonal mean DARF values at the TOA, at the SUR, and in the ATM, along with the AHR values, are shown in Fig. 8b. The seasonal mean TOA forcing values of −21.9, −31.5, and −30.0 W m^{-2} and SUR forcing values of −74.6, −109.6, and −125.7 W m^{-2} were observed at Nanjing during autumn, spring, and summer seasons, respectively. The resultant ATM forcing values of +52.8, +78.2, and +95.8 W m^{-2} for the above respective seasons could lead to corresponding AHR values of 1.48, 2.20, and 2.69 K day^{-1}, respectively. This AHR is, however, an indicative value and may not be exact as it is based upon the atmospheric pressure difference (ΔP) between TOA and SUR in which most of the aerosol lies. A relatively large DARF along with a large AHR during the summer suggests a significant influence of absorbing aerosols from the potential emission sources in the region (El-Metwally et al. 2011; Valenzuela et al. 2012; Esteve et al. 2014). However, a relatively low DARF observed during the autumn could be due to the prevailing meteorological conditions that limits the atmospheric boundary layer of the region.

The values obtained for the DARF were highly dependent on the aerosol load and type, increasing as the AOD increases. Thus, it is very useful to define AFE, a quantity independent of the aerosol load that represents the rate at which the atmosphere is forced per unit of AOD (or τ). The monthly and seasonal evolutions of the mean AFE at the SUR and the TOA obtained at this site during the study period are shown in Fig. 8c, d. The AFE ranges from −131 to −156 W m^{-2} τ^{-1} at the SUR and from −26 to −46 W m^{-2} τ^{-1} at the TOA, with mean values of −144.8 ± −7.6 and −36.0 ± 6.6 W m^{-2} τ^{-1}, respectively, for the entire study period. Furthermore, the above

Table 5 Validation of AERONET-derived and SBDART calculated DARF and AFE at the SUR and TOA along with AHR

Month	AERONET-derived DARF				SBDART calculated DARF				AHR
	DARF		AFE		DARF		AFE		
	TOA	SUR	TOA	SUR	TOA	SUR	TOA	SUR	
October 2007	−26.95	−87.90	−63.95	−209.90	−21.85	−74.62	−45.46	−156.36	1.48
March 2008	−36.70	−128.41	−49.39	−182.83	−33.85	−110.35	−41.41	−142.67	2.15
April 2008	−34.60	−119.16	−48.84	−187.32	−31.01	−101.45	−39.55	−146.74	1.98
May 2008	−31.66	−135.60	−40.46	−182.07	−29.52	−117.14	−34.58	−144.37	2.46
June 2008	−32.60	−155.30	−33.63	−194.04	−29.33	−133.69	−26.05	−147.25	2.93
July 2008	−29.39	−151.41	−30.15	−154.81	−32.38	−135.91	−30.76	−130.78	2.91
August 2008	−29.06	−121.57	−37.69	−176.82	−28.21	−107.59	−33.99	−145.43	2.23

Direct aerosol radiative forcing (DARF), aerosol forcing efficiency (AFE), and atmospheric heating rate (AHR) are measured in terms of watts per square meter, watts per square meter per tau, and Kelvin per day, respectively. Here, τ is AOD$_{500}$ and K is temperature in Kelvin degree
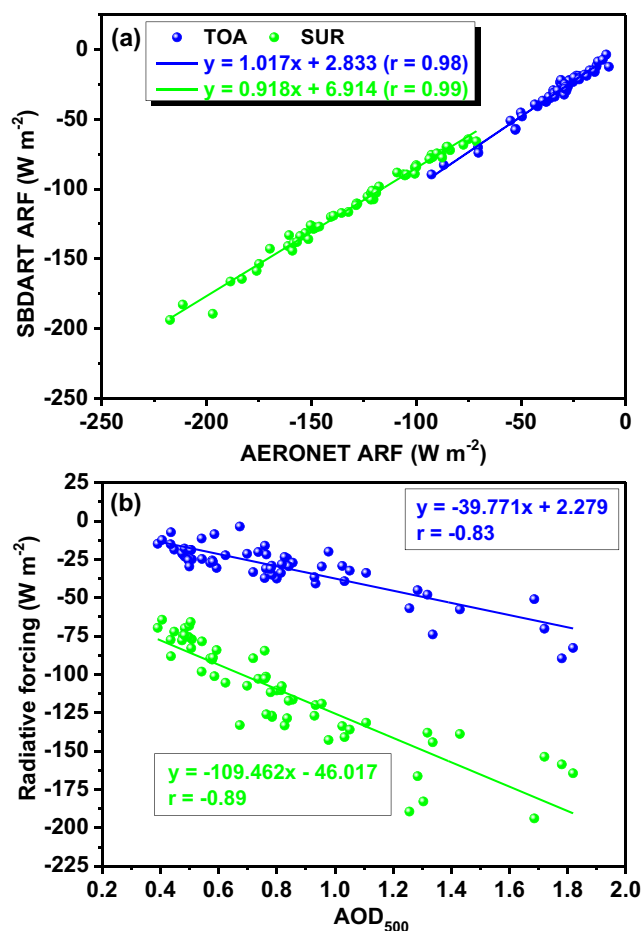
Fig. 9 a Comparison of the AERONET-derived and SBDART computed DARF and (**b**) scatter plot between DARF and AOD_{500} to represent aerosol forcing efficiency at the TOA and the SUR observed at Nanjing during the study period. The *lines* denote the linear regression fitting to the data, and the corresponding obtained regression coefficients and its correlation are also presented

mean AFE value derived in the present study is approximately the same as the one obtained from the linear fits of the DARF at the SUR and at the TOA with the AOD_{500}. Figure 9b shows the linear fits of the DARF estimated at the TOA and the SUR with AOD_{500} obtained at a particular site in Nanjing during the study period. The AFE values, obtained from the slope of these linear fits, were found to be -109.5 ± 46.0 W m$^{-2}\tau^{-1}$ at the SUR and -39.8 ± 2.3 W m$^{-2}\tau^{-1}$ at the TOA.

Aerosol optical properties under dust and haze events: a case study

To compare the differences of the aerosol optical properties under different pollution episodes, we have selected typical dust (low RH) and haze (high RH) events that occurred in Nanjing during the study period. The days have been selected due to the fact that the local atmosphere experienced high aerosol loading and based on the surface measured meteorological data and news

report. Figure 10 shows the variations of aerosol optical properties measured during the dust (25 April 2008) and haze (12 June 2008) days. AOD_{500} on the dusty day (Fig. 10a) was around 0.9 in the morning, which dropped to around 0.7 in the afternoon, whereas $AE_{440-870}$ was found to be 0.7 in the morning and ~0.5 in the afternoon, indicating that the atmosphere was mainly dominated with the coarse-mode dust particles. Additionally, we searched the natural hazard records from the NASA Earth Observatory (http://earthobservatory.nasa.gov/NaturalHazards/) to check whether there were dust events that could cause the extremely high AOD values during the observation period. We found that there was a dust storm event on 25 April 2008 over north China, with dust plumes captured by the MODIS Terra satellite shown in Fig. 10b. The dust, which reached a maximum on the 25th of April, originated from Mongolia (Gobi Desert) and transported toward the east reaching the measurement site. The dust appeared as a beige swirl over the arid landscape. The pale color of this dust plume was consistent with that of dried wetland soils. In contrast, AOD_{500} varied between 2.0 and 4.0, while $AE_{440-870}$ varied stably around 1.2 during the haze day (Fig. 10e), which indicates that fine-mode particles dominated during the whole day. On 12 June 2008, dense haze was observed over northern China, with intense haze captured by the MODIS Terra satellite (Fig. 10f). The haze was thick enough to obscure the land and water surfaces from space which reduced the air quality and decreased visibility in several parts of north and east China. Thus, it is clear that horizontal visibility increased in the afternoon of both cases due to the decrease of AOD.

To investigate the aerosol sources under dust and haze conditions, the Hybrid Single-Particle Lagrangian Integrated Trajectory (HYSPLIT) model (Draxler and Rolph 2003) was adopted to carry out 5-day back-trajectory analyses at three different heights of 500, 1500, and 3000 m above ground level (AGL). The derived trajectories showed different transportation pathways on the dust and haze days. On dusty day, the air masses at all levels originated from Russia, Kazakhstan, and Mongolia, traveled through northern China before reaching the site in Nanjing (Fig. 10c). These trajectory air mass pathways brought a lot of dust aerosols toward the measurement site resulting in high AOD and low AE (coarse particles). Figure 10g shows that the air masses at higher altitudes (1000 and 3000 m AGL) reached Nanjing on 12 June which originated from northeast China and passed through the Yellow Sea and the YRD, while the air masses at 500 m AGL originated from the YRD and traveled back to the Yellow Sea, before reaching the measurement location. Compared with the dust case on the 25th of April, the air masses moved slowly on haze day, which might bring a large number of fine-mode particles, produced from the industrial
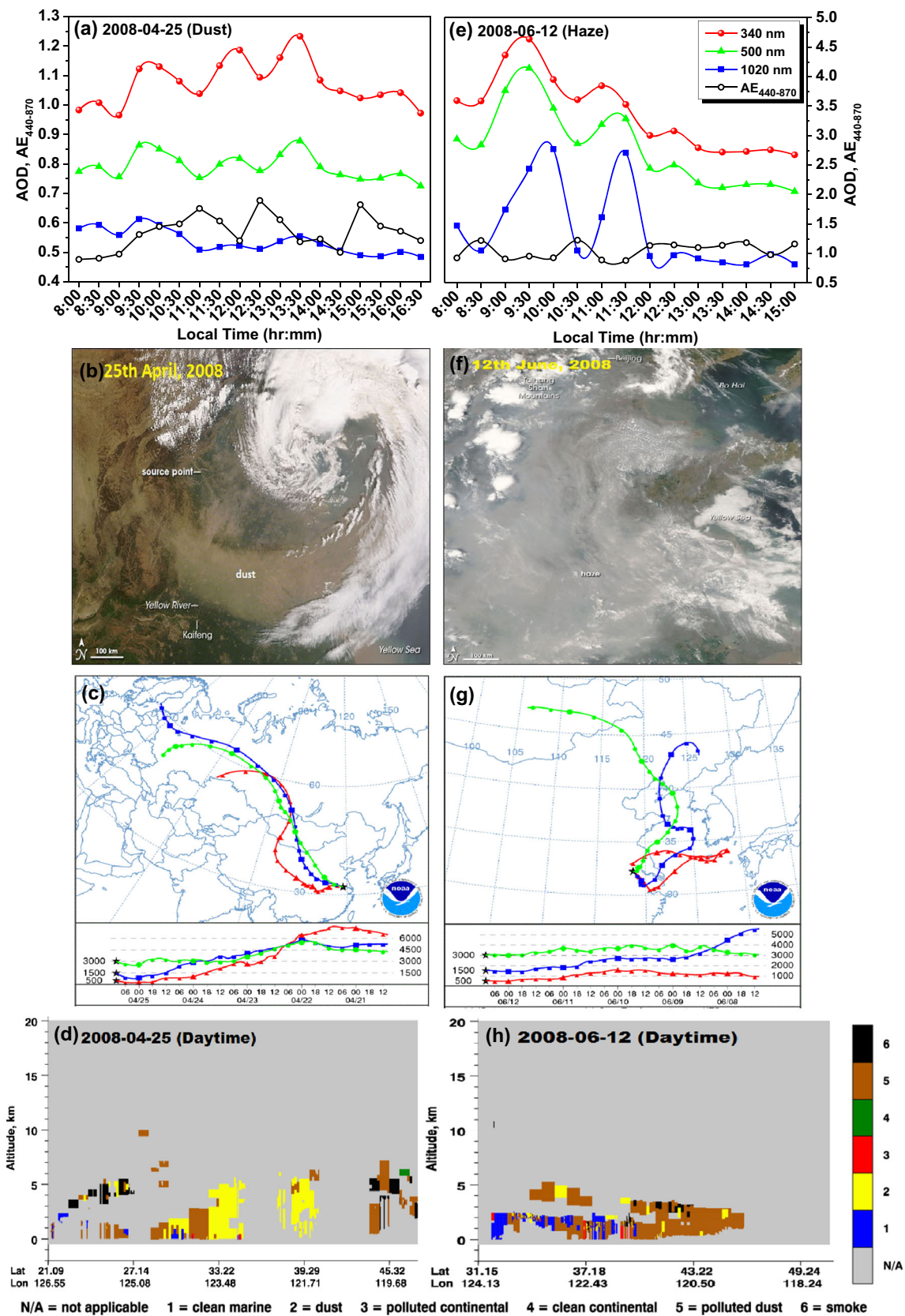
Fig. 10 Aerosol optical properties for a typical/selected **a–d** dust and **e–h** haze episodes during the study period. **a, e** Diurnal AOD at three spectral regions; **b, f** MODIS Terra true color images; **c, g** 5-day HYSPLIT model back-trajectories ending at 1000 UTC over Nanjing at different altitudes; and **d, h** CALIPSO retrieved aerosol subtype profile during dust (25th April, 2008) and haze (12th June, 2008) days

and urban centers of east China, in particular the YRD region to the measurement station.

Also, the aerosol subtypes identified by Cloud-Aerosol Lidar and Infrared Pathfinder Satellite Observation (CALIPSO) (www-calipso.larc.nasa.gov) in the vicinity of the study region include both dust and polluted dust (mainly of coarse-mode particles), but dust aerosols were dominant with lesser contribution from the polluted (anthropogenic) aerosols on dust day (Fig. 10d). On the haze day, the CALIPSO aerosol subtype profile indicated a thick layer of polluted dust extending from the surface to an altitude of about 2 km, which played a substantial contribution to the dense haze pollution (Fig. 10h). This clearly shows that the high AOD and high AE (dominance with fine particles) on the haze day are due to the transport of aerosols from anthropogenic polluted regions in the YRD (Cheng et al. 2015; Yu et al. 2016a).

Summary and conclusions

Column-integrated aerosol optical properties and radiative forcing at Nanjing, an urban-industrial city in the YRD region of China, were analyzed based on the direct sun and almucantar retrievals of sun photometer measurements during September 2007–August 2008. The results reveal that the monthly averaged values of AOD_{500} and $AE_{440-870}$ varied from 0.62 to 1.62 and from 0.95 to 1.25, with an annual mean of 0.95 ± 0.41 and 1.10 ± 0.21, respectively. The AOD_{500} showed a significant seasonal variation, with higher mean values in summer (1.18 ± 0.63) followed by spring (0.83 ± 0.46) and lower in autumn (0.80 ± 0.48). High AOD in summer was associated with anthropogenic aerosols from stagnant weather conditions, secondary aerosol formation under high temperature, increased human activities such as agricultural biomass burning, and hygroscopic growth of aerosols due to enhanced RH with increased columnar PWV. A higher AOD in spring at this site was generally attributed to the long-range transport of dust aerosols upwind from desert source regions, or local dust emissions associated with the dominance of coarse particles (lower AE). The scatter plot of AOD versus AE and AAE versus EAE showed that the dominant aerosol types are mixed and biomass burning/urban-industrial at Nanjing. It is also confirmed from the graphical scheme proposed by Gobbi et al. (2007) that the measurement site could be affected by anthropogenic fine- and coarse-mode dust particles. From the spectral curvature obtained from the second-order polynomial fit, it depicts higher contribution of fine-mode aerosols dominating the aerosol size distribution.

The aerosol volume size distribution depicted that the maximum peak of fine and coarse modes occurred at a radius of 0.2 μm in summer and 3.0 μm in spring, respectively. SSA showed strong seasonal and wavelength dependence over Nanjing. An increase (decrease) in SSA with wavelength was observed in spring (summer) which is attributed to the presence of coarse-mode (fine) dust particles, which are scattering (absorbing) in nature. This is in agreement with the values of real and imaginary parts of complex RI measured at Nanjing. The averaged values of DARF at the TOA and the SUR were estimated to be -29.5 ± 3.8 and -112 ± 20.8 W m^{-2}, respectively, with the atmospheric forcing of 82.1 ± 18.3 W m^{-2}, resulting in an atmospheric heating rate of 2.31 ± 0.52 K day^{-1}. Larger negative DARF at the SUR and lower DARF at the TOA may result in a strong cooling effect at the surface but heating in the atmosphere of Nanjing. This could further impact the regional climate, which needs continued work.

References

Adesina AJ, Kumar KR, Sivakumar V, Griffith D (2014) Direct radiative forcing of urban aerosols over Pretoria (25.75°S, 28.28°E) using AERONET Sunphotometer data: first scientific results and environmental impact. J Environ Sci 26:2459–2474

Alam K, Trautmann T, Blaschke T (2011) Aerosol optical properties and radiative forcing over mega-city, Karachi. Atmos Res 101:773–782

Alam K, Trautmann T, Blaschke T, Majid H (2012) Aerosol optical and radiative properties during summer and winter season over Lahore and Karachi. Atmos Environ 50:234–245

Angstrom A (1964) The parameters of atmospheric turbidity. Tellus 16:64–75

Brock CA, Wagner NL, Anderson BE, Beyersdort A et al (2015) Aerosol optical properties in the southeastern United States in summer—part 2: sensitivity of aerosol optical depth to relative humidity and aerosol parameters. Atmos Chem Phys Discuss 15:31471–31499

Charlson RJ, Schwartz SE, Hales JM, Cess RD, Coakley JA, Hansen JE et al (1992) Climate forcing by anthropogenic aerosols. Science 255:423–430

Che H, Zhang XY, Chen HB, Damiri B, Goloub P, Li ZQ, Zhang XC, Wei Y, Zhou HG, Dong F, et al (2009) Instrument calibration and aerosol optical depth validation of the China aerosol remote sensing network. J Geophys Res 114

Che H, Xia X, Zhu J, Wang H, Wang Y, Sun J, Zhang X, Shi G (2014) Aerosol optical properties under the condition of heavy haze over an

17551

urban site of Beijing, China. Environ Sci Pollut Res. doi:10.1007/s11356-014-3415-5

Che H, Zhao H, Wu Y, Xia X, Zhu J, Dubovik O et al (2015) Application of aerosol optical properties to estimate aerosol type from ground-based remote sensing observation at urban area of northeastern China. J Atmos Solar Terres Phys 132:37–47

Chen J, Jiang H, Wang B et al (2012) Aerosol optical properties from sun photometric measurements in Hangzhou district, China. Int J Remote Sens 33:2451–2461

Cheng T, Xu C, Duan J, Wang Y et al (2015) Seasonal variation and difference of aerosol optical properties in columnar and surface atmospheres over Shanghai. Atmos Environ 123:315–326

Deng J, Wang T, Jiang Z et al (2012) Characterization of visibility and its affecting factors over Nanjing, China. Atmos Res 101:681–691

Di Sarra A, di Biagio C, Meloni D, Monteleone F, Pace G, Pugnaghi S, Sferlazzo D (2011) Shortwave and longwave radiative effects of the intense Saharan dust event of 25–26 March 2010 at Lampedusa (Mediterranean Sea). J Geophys Res 116:D23209. doi:10.1029/2011JD016238

Draxler RR, Rolph GD (2003) HYSPLIT (Hybrid Single-Particle Lagrangian Integrated Trajectory). Model access via the NOAA ARL READY Website. NOAA Air Resources Laboratory, Silver Spring, MD, http://www.arl.noaa.gov/ready/hysplit4.html

Dubovik O, King MA (2000) A flexible inversion algorithm for retrieval of aerosol optical properties from Sun and sky radiance measurements. J Geophys Res 105:20673–20696

Dubovik O, Holben BN, Eck TF, Smirnov A, Kaufman YJ, King MD, Tanre D, Slutsker I (2002) Variability of absorption and optical properties of key aerosol types observed in worldwide locations. J Atmos Sci 59:590–608

Eck TF, Holben BN, Reid JS, Dubovik O, Smirnov A, O'Neill NT, Slutsker I, Kinne S (1999) Wavelength dependence of the optical depth of biomass burning, urban, and desert dust aerosols. J Geophys Res 104. http://dx.doi.org/10.1029/1999JD900923

Eck TF, Holben BN, Dubovik O, Smirnov A, Glob P, Chen HB, et al (2005) Columnar aerosol optical properties at AERONET sites in central eastern Asia and aerosol transport to the tropical mid-Pacific. J Geophys Res 110. http://dx.doi.org/10.1029/2004JD005274

El-Metwally M, Alfaro SC, Wahab MMA, Favez O, Mohammed Z, Chatenet B (2011) Aerosol properties and associated radiative effects over Cairo (Egypt). Atmos Res 99:263–276

Esteve AR, Estelles V, Utrillas MP, Martinez-Lozano JA (2014) Analysis of the aerosol radiative forcing over a Mediterranean urban coastal site. Atmos Res 137:195–204

Giles DM, Holben BN, Eck TF, Sinyuk A, Smirnov A, Slutsker I, et al (2012) An analysis of AERONET aerosol absorption properties and classifications representative of aerosol source regions. J Geophys Res 117. http://dx.doi.org/10.1029/2012JD018127

Gobbi GP, Kaufman YJ, Koren I, Eck TF (2007) Classification of aerosol properties derived from AERONET direct sun data. Atmos Chem Phys 7:453–458

Goloub P, Li Z, Dubovik O, Blarel L, Podvin T, Jankowiak I, Lecoq R, Deroo C, Chatenet B, Morel JP, Cuevas E, Ramos R (2007) PHOTONS/AERONET sunphotometer network overview: description, activities, results. Proc SPIE 6936, doi:10.117/12.783171

Han Y, Wu YH, Wang T, Xie C, Zhao K, Zhuang BL, Li S (2015) Characterizing a persistent Asian dust transport event: optical properties and impact on air quality through the ground-based and satellite measurements over Nanjing, China. Atmos Environ 115:304–316

Holben BN, Eck TF, Slutsker I, Tanre D, Buis JP, Setzer A et al (1998) AERONET—a federated instrument network and data archive for aerosol characterization. Remote Sens Environ 66:1–16

IPCC (2013) Climate change 2013: the physical science basis: contribution of Working Group I to the Fifth Assessment Report of the Intergovernmental Panel on Climate Change. Stocker TF, Qin D, Plattner GK, Tignor M, Allen SK, Boschung J, Nauels A, Xia Y,

Bex V, Midgley PM (eds) Cambridge University Press, Cambridge, pp. 1535

Jacobson MZ (2001) Strong radiative heating due to mixing state of black carbon in atmospheric aerosols. Nature 409:695–697

Kaskaoutis DG, Badarinath KVS, Kharol SK, Sharma AR, Kambezidis HD (2009) Variations in the aerosol optical properties and types over the tropical urban site of Hyderabad, India. J Geophys Res 114: D22204. http://dx.doi.org/10.1029/2009JD012423

Kaskaoutis DG, Sinha PR, Vinoj V, Kosmopoulos PG, Tripathi SN, Misra A, Sharma M, Singh RP (2013) Aerosol properties and radiative forcing over Kanpur during severe aerosol loading conditions. Atmos Environ 79:7–19

Kedia S, Ramachandran S, Holben BN, Tripathi SN (2014) Quantification of aerosol type, and source of aerosols over the Indo-Gangetic plain. Atmos Environ 98:607–619

Kim S-W, Choi I-J, Yoon S-C (2010) A multiyear analysis of clear-sky aerosol optical properties and direct radiative forcing at Gosan, Korea (2001–2008). Atmos Res 95:279–287

Kumar KR, Sivakumar V, Reddy RR, Gopal KR, Adesina AJ (2013) Inferring wavelength dependence of AOD and Angstrom exponent over a sub-tropical station in South Africa using AERONET data: influence of meteorology, long-range transport and curvature effect. Sci Total Environ 461–462:397–408

Kumar KR, Sivakumar V, Reddy RR, Gopal KR, Adesina AJ (2014) Identification and classification of different aerosol types over a subtropical rural site in Mpumalanga, South Africa: Seasonal variations as retrieved from the AERONET Sunphotometer. Aerosol Air Qual Res 14:108–123

Kumar KR, Yin Y, Sivakumar V, Kang N, Yu X, Diao Y, Adesina AJ, Reddy RR (2015) Aerosol climatology and discrimination of aerosol types retrieved from MODIS, MISR, and OMI over Durban (29.88°S, 31.02°E), South Africa. Atmos Environ 117:9–18

Li S, Wang TJ, Xie M, Han Y, Zhuang BL (2015) Observed aerosol optical depth and angstrom exponent in urban area of Nanjing, China. Atmos Environ 123:350–356

Liou KN (2002) An introduction to atmospheric radiation. Elsevier, New York, p 583

Liu J, Zheng Y, Li Z, et al (2012) Seasonal variations of aerosol optical properties, vertical distribution and associated radiative effects in the Yangtze Delta region of China. J Geophys Res 117:D00K38. http://dx.doi.org/10.1029/2011JD016490

Pace G, di Sarra A, Meloni D, Piacentino S, Chamard P (2006) Aerosol optical properties at Lampedusa (central Mediterranean). 1. Influence of transport and identification of different aerosol types. Atmos Chem Phys 6:697–713

Pan L, Che H, Geng F et al (2010) Aerosol optical properties based on ground measurements over the Chinese Yangtze Delta Region. Atmos Environ 44:2587–2596

Pathak B, Subba T, Dahutia P, Bhuyan PK, Moorthy KK, Gogoi MM, Babu SS, et al (2015) Aerosol characteristics in north-east India using ARFINET spectral optical depth measurements. Atmos Environ. doi:10.1016/j.atmosenv.2015.07.038

Ramachandran S, Kedia S (2012) Radiative effects of aerosols over Indo-Gangetic plain: environmental (urban vs rural) and seasonal variations. Environ Sci Pollut Res 19:2159–2171

Ramanathan V, Crutzen PJ, Kiehl JT, Rosenfeld D (2001) Aerosols, climate, and the hydrological cycle. Science 294:2119–2124

Remer LA, Kaufman YJ, Tanre D, Matto S, Chu DA, Martins JV et al (2005) The MODIS aerosol algorithm products, and validation. J Atmos Sci 62:947–973

Ricchiazzi P, Yang S, Gautier C, Sowle D (1998) SBDART: a research and teaching software tool for plane-parallel radiative transfer in the earth's atmosphere. Bull Am Meteorol Soc 79:2101–2114

Romero AS, Gonzalez JA, Calbo J, Lorenzo AS, Michalsky J (2016) Aerosol optical depth in a western Mediterranean site: an assessment of different methods. Atmos Res 174–175:70–84

Russell PB, Bergstorm RW, Shinozuka Y, Clarke AD, DeCarlo PF, Jimenez JL, Livingston JM, Redemann J et al (2010) Absorption Angstrom exponent in AERONET and related data as an indicator of aerosol composition. Atmos Chem Phys 10:1155–1169

Saha A, Mallet M, Roger JC, Dubuisson P, Piazzola J, Despiau S (2008) One year measurements of aerosol optical properties over an urban coastal site: effect on local direct radiative forcing. Atmos Res 90:195–202

Satheesh SK, Vinoj V, Moorthy KK (2010) Radiative effects of aerosols at an urban location in southern India: observations versus model. Atmos Environ 44:5295–5304

Schuster GL, Dubovik O, Holben BN (2006) Angstrom exponent and bimodal aerosol size distributions. J Geophys Res 111. http://dx.doi.org/10.1029/2005JD006328

Singh RP, Dey S, Tripathi SN, Tare V, Holben BN (2004) Variability of aerosol parameters over Kanpur city, northern India. J Geophys Res. doi:10.1029/2004JD004966

Sinha PR, Dumka UC, Manchanda RK, Kaskoutis DG, Sreenivasan S, Moorthy KK, Babu SS (2013) Contrasting aerosol characteristics and radiative forcing over Hyderabad, India due to seasonal meso-scale and synoptic scale processes. Quat J Royal Meteorol Soc 139:434–450

Smirnov A, Holben BN, Eck TF, Dubovik O, Slutsker I (2000) Cloud screening and quality control algorithms for the AERONET data base. Remote Sens Environ 73:337–349

Srivastava AK, Ram K, Singh S, Kumar S, Tiwari S (2015) Aerosol optical properties and radiative effects over Manora Peak in the Himalayan foothills: seasonal variability and role of transported aerosols. Sci Total Environ 502:287–295

Takemura T, Nakajima T (2004) Overview of SKYNET and its activities. Optica Pura y Aplcada 37:3303–3308

Tanre D, Kaufman YJ, Holben BN, Chatenet B, Karineli A, Lavenu F, Blarel L, Dubovik O, Remer L (2001) Climatology of dust aerosol size distribution and optical properties derived from remotely sensed data in the solar spectrum. J Geophys Res 106:205–218

Tiwari S, Srivastava AK, Singh AK, Singh S (2015) Identification of aerosol types over Indo-Gangetic Basin: implications to optical properties and associated radiative forcing. Environ Sci Pollut Res. doi:10.1007/s11356-015-4495-6

Twomey SA, Piepgrass M, Wolfe TL (1984) An assessment of the impact of pollution on the global albedo. Tellus 36B:356–366

Valenzuela A, Olmo EJ, Lyamani H, Anton M, Quirantes A, Alados-Arboledas L (2012) Aerosol radiative forcing during African desert dust events (2005–2010) over southeastern Spain. Atmos Chem Phys 12:10331–10351

Wang P, Che H, Zhang X et al (2010) Aerosol optical properties of regional background atmosphere in northeast China. Atmos Environ 44:4404–4412

Wang L, Gong W, Xia X, Zhu J, Li J, Zhu Z (2015) Long-term observations of aerosol optical properties at Wuhan, an urban site in central China. Atmos Environ 101:94–102

Wu Y, Zhu J, Che H, Xia X, Zhang R (2015) Column-integrated aerosol optical properties and direct radiative forcing based on sun photometer measurements at a semi-arid rural site in northeast China. Atmos Res 157:56–65

Xia X, Chen H, Wang P, Zhang W, Goloub P, Chatenet B, Eck TF, Holben BN (2006) Variation of column-integrated aerosol properties in a Chinese urban region. J Geophys Res 111:D05204. http://dx.doi.org/10.1029/2005JD006203

Xia X, Chen H, Goloub P, Zong X, Zhang W, Wang P (2013) Climatological aspects of aerosol optical properties in North China Plain based on ground and satellite remote-sensing data. J Quant Spectro Radiat Transf 127:12–23

Xia X, Che H, Zhu J, Chen H, Cong Z, Deng X et al (2016) Ground-based remote sensing of aerosol climatology in China: aerosol optical properties, direct radiative effects and its parameterization. Atmos Environ 124:243–251

Yu X, Ma J, Kumar KR, Zhu B, An J, He J, Li M (2016a) Measurement and analysis of surface aerosol optical properties over urban Nanjing in the Chinese Yangtze River Delta. Sci Total Environ 546:277–291

Yu X, Kumar KR, Lu R, Ma J (2016b) Changes in column aerosol optical properties during extreme haze-fog episodes in January 2013 over urban Beijing. Environ Pollut 210:217–226

Yu X, Lu R, Kumar KR, Ma J, et al (2016c) Dust aerosol properties and radiative forcing observed in spring during 2001–2014 over urban Beijing, China. Environ Sci Pollut Res. doi:10.1007/s11356-016-6727-9

Zhu J, Xia X, Che H, Wang J, Zhang J, Duan Y (2016) Study of aerosol optical properties at Kunming in southwest China and long-range transport of biomass burning aerosols from North Burma. Atmos Res 169:237–247

Zhuang BL, Wang TJ, Li S, Liu J, Talbot R, Mao HT, Yang XQ et al (2014) Optical properties and radiative forcing of urban aerosols in Nanjing, China. Atmos Environ 83:43–52